National Library of Canada
Bibliothèque nationale du Canada

Canadian Theses Service
Service des thèses canadiennes

Ottawa, Canada
K1A 0N4

NOTICE

The quality of this microform is heavily dependent upon the quality of the original thesis submitted for microfilming. Every effort has been made to ensure the highest quality of reproduction possible.

If pages are missing, contact the university which granted the degree.

Some pages may have indistinct print especially if the original pages were typed with a poor typewriter ribbon or if the university sent us an inferior photocopy.

Previously copyrighted materials (journal articles, published tests, etc.) are not filmed.

Reproduction in full or in part of this microform is governed by the Canadian Copyright Act, R.S.C. 1970, c. C-30.

AVIS

La qualité de cette microforme dépend grandement de la qualité de la thèse soumise au microfilmage. Nous avons tout fait pour assurer une qualité supérieure de reproduction.

S'il manque des pages, veuillez communiquer avec l'université qui a conféré le grade.

La qualité d'impression de certaines pages peut laisser à désirer, surtout si les pages originales ont été dactylographiées à l'aide d'un ruban usé ou si l'université nous a fait parvenir une photocopie de qualité inférieure.

Les documents qui font déjà l'objet d'un droit d'auteur (articles de revue, tests publiés, etc.) ne sont pas microfilmés.

La reproduction, même partielle, de cette microforme est soumise à la Loi canadienne sur le droit d'auteur, SRC 1970, c. C-30.

NL-339 (r. 88/04)

Canada

THE UNIVERSITY OF ALBERTA

AN EVALUATION OF THE YTTRIA-CALCIA SYSTEM AS A POTENTIAL CERAMIC ELECTROLYTE

BY

JONATHON BROWN, B.Sc.

(C)

A THESIS

SUBMITTED TO THE FACULTY OF GRADUATE STUDIES AND RESEARCH

IN PARTIAL FULFILMENT OF THE REQUIREMENTS FOR THE DEGREE OF

MASTER OF SCIENCE

IN

METALLURGICAL ENGINEERING

DEPARTMENT OF MINING, METALLURGICAL AND PETROLEUM ENGINEERING

EDMONTON, ALBERTA

FALL 1988

Permission has been granted to the National Library of Canada to microfilm this thesis and to lend or sell copies of the film.

The author (copyright owner) has reserved other publication rights, and neither the thesis nor extensive extracts from it may be printed or otherwise reproduced without his/her written permission.

L'autorisation a été accordée à la Bibliothèque nationale du Canada de microfilmer cette thèse et de prêter ou de vendre des exemplaires du film.

L'auteur (titulaire du droit d'auteur) se réserve les autres droits de publication; ni la thèse ni de longs extraits de celle-ci ne doivent être imprimés ou autrement reproduits sans son autorisation écrite.

ISBN 0-315-45624-8

THE UNIVERSITY OF ALBERTA

RELEASE FORM

NAME OF AUTHOR: JONATHON BROWN

TITLE OF THESIS: AN EVALUATION OF THE YTTRIA-CALCIA SYSTEM AS A POTENTIAL CERAMIC ELECTROLYTE

DEGREE: MASTER'S OF SCIENCE

YEAR THIS DEGREE GRANTED: 1988

Permission is hearby granted to THE UNIVERSITY OF ALBERTA LIBRARY to reproduce single copies of this thesis and to lend or sell such copies for private, scholarly or scientific research purposes only.

The author reserves all other publication rights, and neither the thesis nor extensive extracts from it may be printed or otherwise reproduced without the author's written permission.

Jonathon Brown
64 Marlboro Dr
Spruce Grove, AB
T7X 2N9

Date: Aug 24/1988

THE UNIVERSITY OF ALBERTA

FACULTY OF GRADUATE STUDIES AND RESEARCH

The undersigned certify that they have read, and recommend to the faculty of Graduate Studies and Research for acceptance, a thesis entitled "AN EVALUATION OF THE YTTRIA-CALCIA SYSTEM AS A POTENTIAL CERAMIC ELECTROLYTE" submitted by JONATHON BROWN in partial fulfilment of the requirements for the degree of MASTER of SCIENCE in METALLURGICAL ENGINEERING.

T. H. Etsell
.....
(Supervisor)

.....

.....

.....

Date: .....

Acknowledgements

The author is indebted to his supervisor Dr. T.H. Etsell for his patience and support throughout this project.

Thanks are also due to the all the technical staff of the Department of Mineral, Metallurgical and Petroleum Engineering. A special thanks must go out to Tina Barker, Shiraz Merali and Jacques Gibeau whose help and tolerance was greatly appreciated.

Finally, the author wishes to thank his father, Dr. T.D. Brown, and Stan Backs for their diligent and perhaps overzealous proof-reading of this work. Additional thanks go out to his fellow graduate students for countless discussions including the occasional ones related to research.

Abstract

Current oxygen sensor technology employs a ceramic electrolyte based on zirconia. Yttria has been proposed as a possible substitute for zirconia. Theory predicts that yttria doped with calcia may possibly serve as an effective electrolyte material.

A study was undertaken to evaluate yttria and yttria-calcia mixtures as potential electrolytes. The study involved a phase study, where the degree of solid solution between Y_2O_3 and CaO was measured using a x-ray diffraction technique; a kinetic study, where the rate of exsolution was studied using an x-ray diffraction technique; and a conductivity study, where the electrical conductivity of the ceramic material was measured using a two probe technique.

The phase study showed a region of solid solubility, based on the C-type structure of yttria, which began at 1400 C and continued up to the highest temperature studied, 2000 C, where 12.4% CaO could be dissolved in Y_2O_3. At lower temperatures (1000 C, 1200 C) there was no solid solubility between the two compounds.

Exsolution kinetics for a Y_2O_3-10%CaO solution showed that the grain boundary precipitation proceeded by a nucleation and growth process. Two distinct regions were observed. In the first (1200-1400 C) the rate of exsolution could be descibed by the following equation:

$$\ln \frac{1}{1-\alpha} = kt^{3.33}$$

and had the following activation energy, 28.6 kJ/mol.

In the second region the rate law was

$$\ln \frac{1}{1 - \alpha} = kt^{2.04}$$

and the activation energy was 159.4 kJ/mol.

The electrical measurements showed that both the pure yttria and the mixed compound exhibit some ionic conductivity over the temperature range 800-1400 C under partial oxygen pressures of $1\text{-}10^{-20}$ atm. The Y_2O_3-CaO mixtures showed significant ionic conductivity below 10^{-10}atm, but the presence of electron holes at higher pressures suggests that the material becomes a mixed conductor.

TABLE OF CONTENTS

CHAPTER		PAGE
I	INTRODUCTION	1
II	LITERATURE SURVEY	5
	A) Solid Solutions between Rare Earth Oxides and Alkaline Earth Oxides	7
	C-type Rare Earth Oxides and MgO ...	7
	C-type Rare Earth Oxides and CaO ...	9
	C-type Rare Earth Oxides and other Alkaline Earth Oxides	12
	B) The Electrical Conductivity of Y_2O_3 .	13
	C) Exsolution Phenomena in Oxides	19
III	THEORETICAL CONSIDERATIONS	25
	A) Effects of Additives in Oxides	25
	B) Defects in Stoichiometric Oxides	29
	C) Defects in Nonstoichiometric Oxides ..	33
	Oxygen Deficient Oxides	33
	Metal Deficient Oxides	35
	Intrinsic Ionization	36
	D) The Effects of Doping on Defect Structure	37
	Calculating the Defect Concentration.	37
	Simple Defect Equilibria	38
	Complex Defect Equilibria	41
	Defect Structure and Electrical Conductivity	44
	F) Decomposition of Solids	47
	Heterogeneous Nucleation	48

	Nucleation Kinetics	50
IV	EXPERIMENTAL	57
	A) Sample Preparation	57
	B) Phase Study	60
	C) Kinetics of Exsolution	62
	D) Electrical Conductivity	63
V	RESULTS AND DISCUSSION	67
	A) Phase Study	67
	B) Kinetics of Exsolution	74
	C) Electrical Conductivity	85
VI	CONCLUSIONS	94
	References	96
	Appendix I	100

LIST OF TABLES

Table		Page
1	A comparison of thermal shock behavior of various refractory oxides	3
2	Solid state reaction rate equations	24
3	Kroeger-Vink notation for describing crystal defects in a compound AB	27
4	Values of m for nuclei growth models for solid-solid interactions	56
5	Impurities in Y_2O_3 and $CaCO_3$	59
6	Impurities in the high purity material	63
7	The "d" spacings for the 10 most intense x-ray reflections of Y_2O_3 and CaO	71
8	A summary of the solubility limits of CaO in Y_2O_3	72
9	A comparison of the correlation coefficients of the various models	80
10	Summary of the "m" values for the experimental temperature range	80

LIST OF FIGURES

Figure		Page
1	Self-diffusion coefficients for oxygen and yttrium in yttria	4
2	The C-type rare earth structure	6
3	One of the two possible coordination groups	6
4	Proposed phase diagrams for rare earths and CaO	10
5	Summary of conductivity data for pure yttria	17
6	Conductivity data for Y_2O_3-CaO	20
7	Schottky defect in an oxide MO	30
8	Frenkel disorder in an oxide MO	30
9	The critical nucleus size for grain boundary nucleation	49
10	The coprecipitation flowsheet	58
11	The conductivity cell	64
12	A comparison of experimental densities with those predicted by the anion vacancy model	68
13	Variation of the lattice parameter with %CaO	70
14	Modified Y_2O_3-CaO phase diagram	73
15	Decomposition curves for Y_2O_3-CaO at 1200 C - 1500 C	75
16	Decomposition curves for Y_2O_3-CaO at 1600 C - 1800 C	76
17	Comparison of solid state models Zero, D1, D2, R2	77
18	Comparison of solid state models D3, D4, R3	78
19	Comparison of solid state models F1, A2, A3	79
20	Determination of "m" from 1200 - 1500 C	81

21	Determination of "m" from 1200 - 1500 C ...	82
22	Arrhenius plot for the Y_2O_3-CaO system	84
23	Conductivity isotherms for pure yttria	86
24	Conductivity isotherms for Y_2O_3-5%CaO	87
25	Conductivity isotherms for Y_2O_3-5%CaO	88
26	The dependence of the "p" type conductivity on the partial oxygen pressure	90
27	Arrhenius plots for total conductivity	93

I. INTRODUCTION

Electrolytic conduction was first discovered in a solid oxide material by Nernst[1] at the turn of the century. His early work with zirconia (ZrO_2) stood for forty years until Wagner and Kiukkola[2,3] defined the defect structure of calcia-stabilized zirconia and determined its electrolytic behaviour. These authors also demonstrated a practical use for the solid electrolyte by using it in an oxygen concentration cell to make thermodynamic measurements. Later, diffusion and conductivity measurements confirmed that conduction of the oxygen ion through the solid was, in fact, the transport mechanism in the solid.[4]

Since that time, research into solid oxide electrolytes has increased substantially. While other oxides, most notably thoria and ceria, have been used as oxygen ion conductors, the zirconia-based solid electrolyte remains the most successful.

Experimental success with zirconia has led to a successful transfer to industry. The electrolyte can be used as a high temperature fuel cell, for the electrolysis of water, and to make thermodynamic measurements. The most significant metallurgical application is the determination of the dissolved oxygen content in molten metals. Despite the success found with using the zirconia based electrolyte for measuring oxygen activity in liquid metals, problems do exist. These problems include chemical attack of the cell

components, sensitivity to thermal shock, and electronic conduction in the electrolyte at low oxygen activities.

By identifying the problems associated with the zirconia-based electrolyte, we can outline some criteria needed to evaluate a potential new solid electrolyte material as a suitable oxygen sensor[5]:

1) The electrolyte must be capable of withstanding the extreme thermal shock that develops when it is placed in a molten metal.

2) The electrolyte must remain impervious to gaseous oxygen.

3) The electrolyte must be thermodynamically stable at high temperatures, and stable in the presence of both the liquid metal and any accompanying slag. In addition the electrolyte must be inert with respect to the electrode material.

4) The electrolyte should remain an ionic conductor at oxygen partial pressures down to approximately 10^{-15} atmospheres in order that the oxygen concentration, of steel, can be determined down to about 1 ppm .

The structural similarities between zirconia and yttria and their proximity on the periodic table has led to yttria's candidacy as a possible electrolyte material. Pure yttria has been shown to meet the first three criteria outlined above. Its thermal shock behaviour is comparable to that of zirconia and other refractory oxides (Table 1). Powdered yttria can be sintered to form simple shapes with

densities greater than 95% of the theoretical density. Finally, yttrium is very similar to the rare earth elements, and its oxide is well-known for its chemically inert behaviour. In addition, the self-diffusion coefficients of the Y^{3+} and O^{2-} ions also suggest that yttria may be a suitable oxygen ion conductor. The diffusion coefficient of oxygen in yttria is 2-3 orders of magnitude higher than the diffusion coefficient of yttrium in yttria[7-10] (Figure 1).

Table 1. A comparison of the thermal shock behaviour of various refractory oxides[9].

Oxide	Young's Modulus (E) GN/m^2	Coefficient of Thermal Expansion (α) x 10^6 /°C	Poisson's Ratio* (μ)	Thermal Stress** (σ) GN/m^2
Y_2O_3	166.5	9.3	0.35	$2.3 \times 10^{-3} \Delta T$
ZrO_2	185.4	8.0	0.36	$2.3 \times 10^{-3} \Delta T$
Al_2O_3	380.5	7.5	0.37	$4.5 \times 10^{-3} \Delta T$
MgO	295.2	12.6	0.33	$5.5 \times 10^{-3} \Delta T$

* -Poisson's ratio for yttria is an average of the Poisson's ratio for the other three oxides

** -Where the thermal stress, as a first approximation is $\sigma = E\alpha\Delta T/(1-\mu)$ as defined by Faber et al.[11]

The objective of this research was to determine the suitability of yttria doped with calcia as a ceramic electrolyte for use at high temperatures.

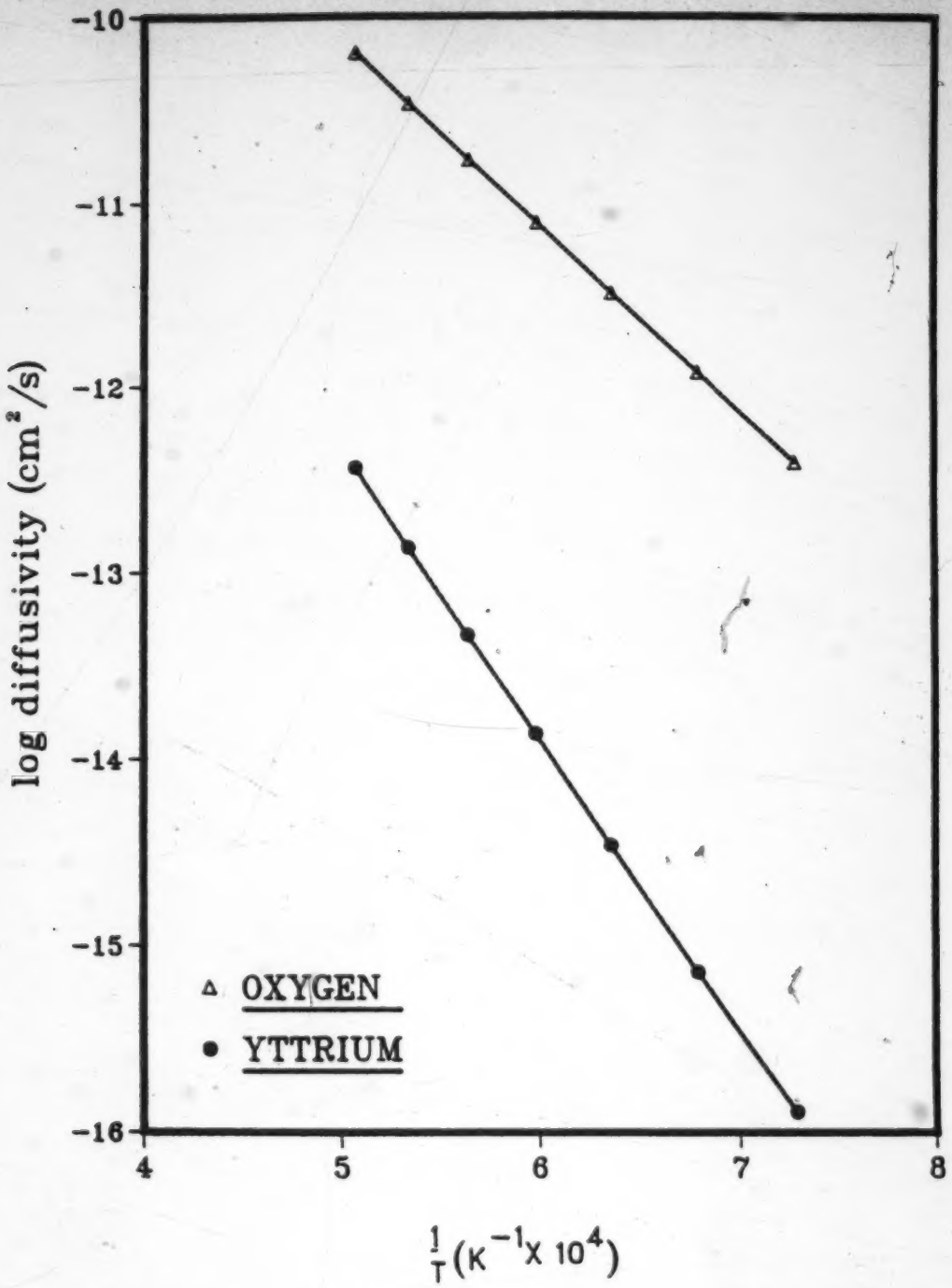

Figure 1. Self-diffusion coefficients for oxygen[8] and yttrium[18] in yttria.

II. LITERATURE SURVEY

At temperatures below 2300 C[13] yttria has the C-type rare earth structure. The C-type structure can best be described as a modified fluorite structure (the structure of cubic ZrO_2 and several other oxygen ion conductors). As decribed by Paton[13] the structure has eight yttrium ions at the "special" position (1/4 1/4 1/4), the remaining 24 cations occupy the sites (1,0,1/4). The 48 oxygen ions are in the general positions (x,y,z) and are arranged in a distorted tetrahedra, where a tetrahedra has a coordination number of 4, around the yttrium ions, the yttrium-oxygen bonding distances being unequal. This structure is represented in Figures 2 and 3.

Above 2300 C the crystal structure of the compound changes; that is, it undergoes a series of polymorphic transformations as the temperature increases. Yttria can exist in a monoclinic (B), hexagonal(H), or a second cubic (X) crystal arrangement.

Each yttrium cation has a coordination number of six and its coordination geometry can be described by one of two distorted tetrahedra[14]. The first type of tetrahedra comprises one quarter of all the arrangements in which two oxygen atoms are missing along the body diagonal. In the remaining three quarters of the tetrahedra the oxygen atoms are missing along the face diagonal (Figure 3). This creates paths for oxygen atom travel along the <111> directions. It is anticipated that these paths, along with

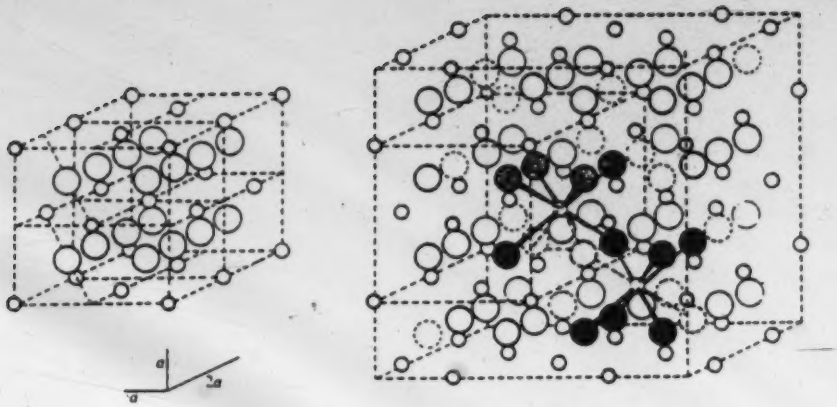

Figure 2. The C-type rare earth structure (right) showing its relationship to the calcium fluorite structure[14]. The anion is represented as the larger of the two atoms.

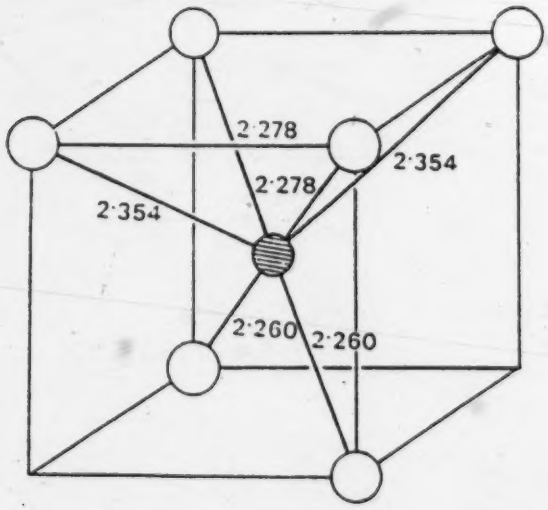

Figure 3. One of the two possible coordination arrangements found in the C-type structure[13]. The interatomic distances are shown in angstroms.

the oxygen vacancies created by the formation of a solid solution between yttria and calcia, will promote ionic conductivity.

A) Solid Solutions between Rare Earth Oxides and Alkaline Earth Oxides

The interaction of oxides of the rare earth elements with highly refractory oxides of other groups of the periodic system is one of the less studied areas of high temperature chemistry[15]. If we only consider the rare earth oxides that have the C-type structure, the amount of available information is reduced still further. Other rare earth structures are hexagonal (A) and monoclinic (B). The rare earth oxides that can exist in the C-type structure start with Nd_2O_3 and continue through the rare earth oxides until Lu_2O_3, a total of twelve. Yttrium and scandium, while not strictly rare earth metals, are often included in this category because of their similarity to the rare earths. In this thesis, the term "rare earth" shall refer to the lanthanide series of elements plus the group III transition metals, (especially yttrium).

Interactions between the rare earth oxides and the alkaline metal oxides have not been studied for all the possible rare earths. Only Y_2O_3, Yb_2O_3, Sc_2O_3, Dy_2O_3, and Gd_2O_3 have been reacted with the alkaline earth oxides, generally MgO or CaO.

C-type Rare Earth Oxides and MgO

The phase diagram associated with Sc_2O_3 and MgO has

been determined by two different techniques. Lopato[16] used differential thermal analysis, an annealing and quenching method, and the theory of regular solutions to determine the form of the phase diagram. While each method provided slightly different locations for significant points, the diagram was a eutectic type - the liquid produced the two original solids (with some solubility of one in the other) and showed no compound formation. Similar phase diagrams were proposed for the systems Y_2O_3-MgO, Er_2O_3-MgO, and Yb_2O_3-MgO [17]. The melting point at the eutectic composition was seen to increase with the increasing atomic number of the rare earth element involved with the C-type oxide.

With certain oxides there are, however, some distinctive features. For example, in the systems containing cerium oxide, there is no evidence of a rare earth based solid solution. Consequently, the transition temperatures for the polymorphic transformations are not affected.

With the C-type oxides from Dy_2O_3 to Yb_2O_3 and including Y_2O_3, adding MgO can lower the transition temperature 20 - 50 C. In the case of Y_2O_3 - MgO, the cubic to monoclinic transformation temperature drops approximately 20 C [18].

Solid solutions between MgO and the rare earth oxides exist when the ionic radii of the two cations are similar in size. The degree of solubility is limited, generally below 1% at 1600 C but can increase substantially at higher

temperatures (e.g. 30 atomic % in Sc_2O_3 at 2240 C)

C-type Rare Earth Oxides and CaO

The literature on these systems is somewhat more substantial than that for MgO-rare earth systems. Lopato, after studying three systems (Dy_2O_3-CaO, Y_2O_3-CaO, and Yb_2O_3-CaO)[10], described the principal features of these systems (Figure 4). Firstly, there existed three distinct compounds: $CaLn_4O_7$, $CaLn_2O_4$, and $Ca_3Ln_2O_6$ where Ln was any of the rare earths examined. An additional compound, $Ca_2Yb_2O_5$, was observed in the system involving ytterbium oxide. Secondly, regions of solid solutions existed at both the rare earth-rich and CaO-rich ends of the phase diagrams. Thirdly, their was a decrease in the phase transition temperature of the rare earth oxide in the presence of CaO.

Not all of the compounds mentioned above are present in every system. Barry[20], for example, in his study of the Gd_2O_3-CaO system, only observed the compound $CaGd_2O_7$. This system also failed to show any solid solubility in either the C-type structure at temperatures below 1150 C, or in the B-type arrangement at higher temperatures.

Compound formation in the system CaO-Yb_2O_3 has been studied extensively by Barry[20]. The existence of the four crystalline compounds described by Lopato, was confirmed above 1850 C. The metastable $CaYb_4O_7$ compound was observed only upon extremely rapid quenching from the melt.

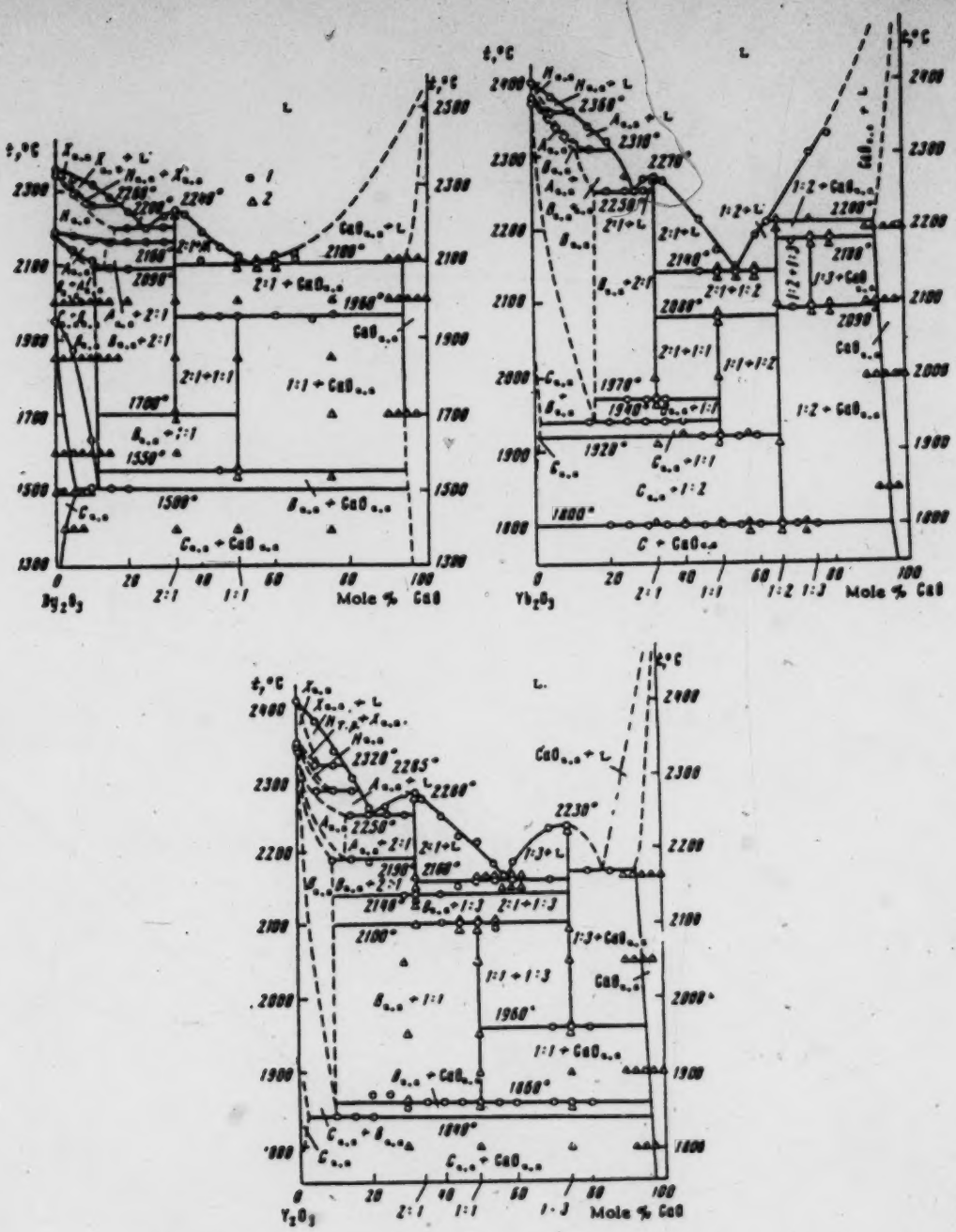

Figure 4. Proposed phase diagrams for rare earths and CaO[19].
(Note the dotted lines in the solid solution region indicating uncertainty)

While MgO was seen to lower the polymorphic transition temperature only slightly (20 - 50 C), CaO had a somewhat more substantial effect. In the rare earth oxide series from Tb_2O_3 to Yb_2O_3 (including Y_2O_3), a stabilization of the solid solutions based on the B-type structure occurs. In the case of the Dy_2O_3-CaO system the transition temperature for the cubic to monoclinic transformation drops from 1900 C in pure Dy_2O_3 to 1600 C when 25 atomic percent CaO is added[21]. Lopato[19] has tentatively suggested similar behaviour in the Y_2O_3-CaO and Yb_2O_3-CaO systems, but the degree of solid solution is much less and the consequent change in the transition temperature is not as substantial.

In the case of Yb_2O_3, the monoclinic arrangement exists above 1950 C and permits a small amount of solid solubility. Lopato also indicates a slight degree of solid solubility in the C-type structure (2 % at 1900 C). This is in direct contrast to the results of other authors[20] who failed to find any solid solubility in either form of the oxide. Although several works agree on the existence of a region of solid solubility in these systems, there is little agreement on the boundaries of the region. In the Y_2O_3-CaO system, for example, Lopato[19] identified a region of solid solubility based on the C-type modification of Y_2O_3 beginning at 1775 C and ending at 1925 C with a maximum of 3% CaO being dissolved in the Y_2O_3. Etsell[22], however, was able to achieve as much as 5% solubility at

1600 C using a co-precipitation technique to prepare the powders.

C-type Rare Earth Oxides and other Alkaline Earth Oxides

Of the remaining alkaline earth metals, only the oxides of Ba and Sr have been the subject of phase studies with oxides of rare earths. These studies have been generally directed towards identifying the structure and the optical properties of the equimolar compound. A few studies involving other compositions do, however, exist and Lopato jointly with Maister and Shvchenko[23] have analyzed these systems. When mixed with C-type rare earth oxides, BaO went through the same transformations as noted earlier for CaO. When mixed with Y_2O_3 or Yb_2O_3, only a very small region of solid solubility (based on the C-type structure) was observed. In both cases, the limit of the solubility was 2% BaO dissolved in the rare earth oxide and this was observed only at very high temperatures (above 2000 C). The addition of BaO was not seen to lower the transformation temperature nearly as much as the addition of CaO. Drops of approximately 50 C were seen for Y_2O_3 and of 100 C for Yb_2O_3.

The systems Y_2O_3-BaO and Yb_2O_3-BaO differed in terms of the compounds that existed between the component oxides. While both systems showed a congruently melting compound containing 60% BaO, the Y_2O_3 system also showed a 1:1 BaO:Y_2O_3 compound at temperatures below 1400°C.

Both of the compounds mentioned above existed when BaO

was in equilibrium with Dy_2O_3 [24]. Again the 1:1 equimolar compound existed only at the lower temperatures. As in similar systems, the addition of the alkaline earth oxide barely reduced the transition temperature. An addition of 2% BaO (the solubility limit) lowered the transition temperature by 50 C.

The addition of SrO to Y_2O_3 or Yb_2O_3 did not produce any different effects[25]. Only limited solid solubility existed in any of the forms of the rare earth oxides and once again only at high temperatures (greater than 2000 C).

The research directed towards defining the phase diagrams involving rare earth oxides and alkaline earth oxides has been sparse. Even when a specific system has had concentrated attention, the results of different authors often have been contradictory in one manner or another.

In addition the vast majority of the work has been performed using a static quench method. Recent advances have been able to improve on this technique. However, despite the apparent benefits of new techniques such as super rapid quenching, hydrothermal synthesis, high temperature x-ray diffraction, and super high pressure methods, recent papers by Lopato[26,27] have failed to reveal any new infomation regarding C-type rare earth oxides in equilibrium with alkaline earth oxides.

B) The Electrical Conductivity of Y_2O_3

When an oxide is exposed to an electrical field both electronic and ionic charge carriers can migrate.

Electrical conductivity results from the field-induced motion of both types of charged species. Electronic conductivity results from the movement of electrons and electron holes; ionic conductivity results from the movement of ions. Since electrons and electron holes are much more mobile than either anions or cations, the presence of even small amounts of electronic defects will result in electronic conduction. Consequently, the majority of materials are electronic conductors. A conductor can be solely an electronic conductor, have significant contributions from both electronic and ionic carriers (a mixed conductor), or be solely an ionic conductor. Regardless of whether a material is an electronic or ionic conductor, usually only one of the conducting species (electron, electron hole, anion, or cation) will carry the majority of the charge.

Electronic materials can be classified as either "n" or "p" type semi-conductors. An "n" type conductor is one where a negatively charged species (electrons) carries most of the charge; a "p" type conductor uses the positively charged species (electron holes). It is possible to change the mode of conduction ("n"-type or "p"-type) by changing the conditions to which the material is exposed.

In general, ionic conductivity is controlled by the motion of ions in either the cation or the anion sublattice. The defect structure of a material thus becomes critical with regards to all types conductivity. It has

been observed that very small changes in stoichiometry can lead to significant changes in the total electrical conductivity of a compound.

The defect structure of pure yttria was first investigated by Tallon and Vest[28] who measured the electrical conductivity of the oxide. They determined that the most probable point defects (at temperatures between 1200 C and 1600 C and under partial oxygen pressures above 10^{-9} atm) are fully ionized yttrium vacancies (all three outer electrons have left the atom). This was based on their discovery that yttria was a pure electronic conductor within that range. Mixed ionic and electronic conduction was observed below 900 C but the authors did not relate this observation to the defect structure. They did, however, identify the ionic transference numbers (t_{ion}, an indication of the degree of ionic conductivity) as 0.15 at 800 C and 0.30 at 700 C, both at 10^{-15} atm of oxygen.

This result was in agreement with earlier work by Noddack and Walch[29] who suggested that Y_2O_3 was predominantly an electronic conductor over the temperature range 600 C - 1200 C. Later work by Subba Rao et al[30] confirmed the results of Tallon and Vest by successfully reproducing the activation energy associated with conduction.

Using an EMF technique, Tare and Schmalzried[31] identified ionic domain boundaries (i.e., the limits of temperature and pressure within which the material conducts

ionically) associated with conduction at 825 C. They concluded that Y_2O_3 would be an ionic conductor if the logarithm of the partial pressure of oxygen was between -4.2 atm and -21.5 atm; the ionic transference number at 825 C and 10^{-15} atm was 0.975.

McPheeters[32] took advantage of this fact and used a Y_2O_3 solid electrolyte to determine the activity of oxygen in liquid sodium. The calibration curve for the electrolyte included in his patent suggests that for temperatures between 400 and 500 C, the ionic transference number of Y_2O_3 can reach unity if the oxygen activity is very small.

Schieltz et al [33] carried the work of Tare and Schmalzried one step further. Using a similar EMF technique they identified the ionic domain boundaries over a range of temperatures (700 - 1000 C). They discovered a narrow region of mixed ionic conduction (t_{ion} greater than 0.5) but could not identify any region of electrolytic behaviour (t_{ion} greater than 0.99).

An extension of this train of thought was provided by Volchenkova and Zubankova[34], who identified the boundaries not only for ionic conductivity but for other types of conductivity as well. A summary of the conductivity domain data for yttria is shown in Figure 5.

The characteristics of yttria-based compounds and solid solutions have been examined. Yttria-rich oxide mixtures have been examined by Etsell[22], Steele et al[35], Kim et al[36], Uematsu et al[37], Scott[38] , and Biggs[39]. In the

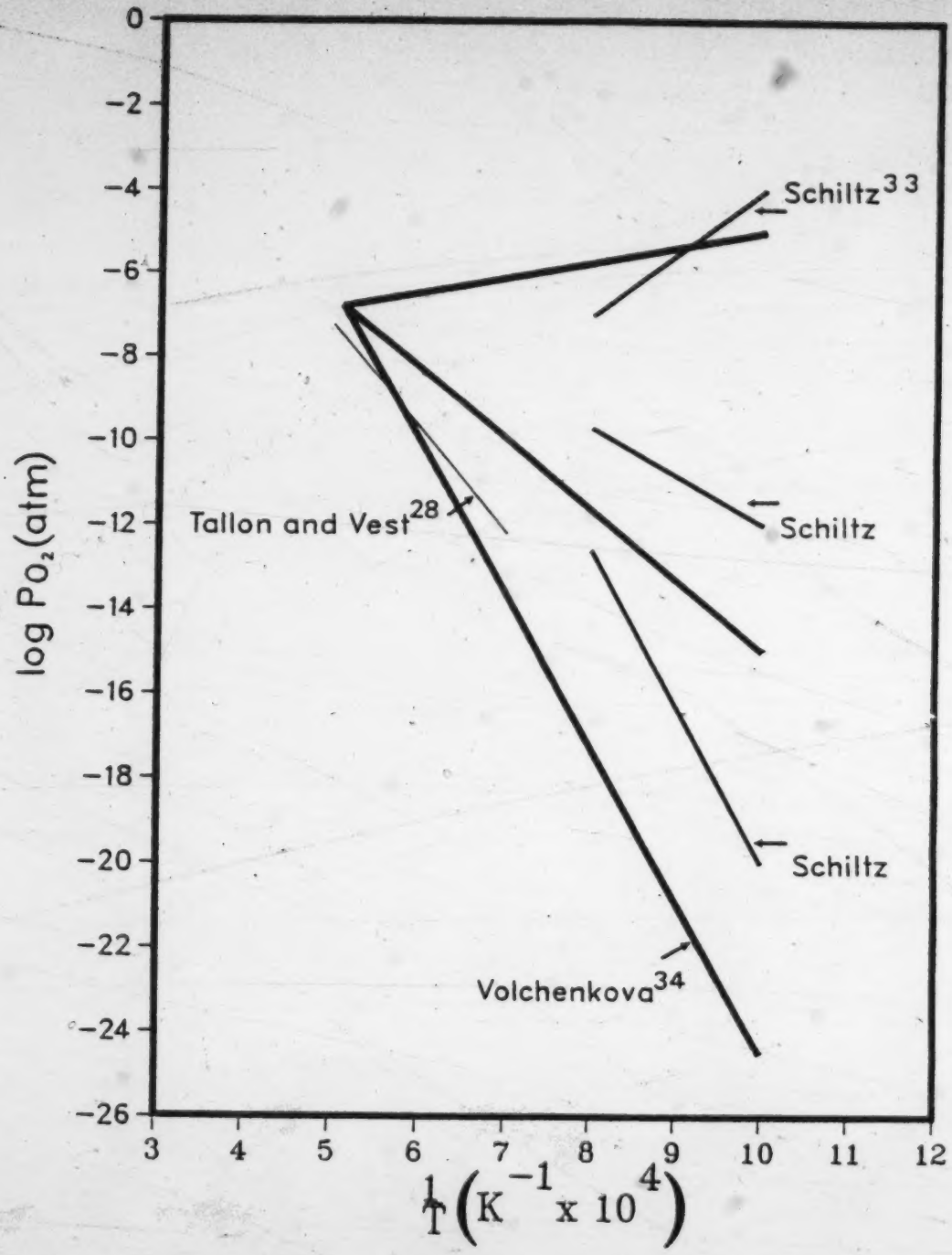

Figure 5. Summary of conductivity data for pure yttria.

cases where the original Y_2O_3 was doped with an ion whose ionic charge was greater than +3 (the valence of a yttrium ion), the ceramic was, in all but one case, seen to demonstrate a region of constant conductivity.

The exception occurred when Y_2O_3 was doped with CeO_2[36]. In this situation, the conductivity was seen to be proportional to the oxygen partial pressure with the actual relationship being temperature dependent. From 500 - 750 C the conductivity was proportional to $Po_2^{1/6}$, whereas from 750 - 1100 C the dependence was $Po_2^{1/5.3}$. It was suggested that the Y_2O_3-CeO_2 system shows mixed ionic and electron hole conduction at low temperatures and electron hole conduction alone at the high temperatures. This indicated a predominance of oxygen interstitial defects at low temperatures and of yttrium vacancies at high ones.

When ThO_2 [37] or TiO_2 [38] was used to dope Y_2O_3, a region of constant conductivity (independent of the oxygen partial pressure) was observed, suggesting an ionic mode of conduction since lattice defect concentrations are only weakly dependent on oxygen pressure. In the case of ThO_2 additions, the ionic region was only apparent at lower temperatures (600-900 C) and slowly disappeared as the temperature increased towards 1400 C. The TiO_2-doped Y_2O_3 maintained its ionic conductivity over the entire range of temperatures studied, 700 - 1000 C.

Studies involving Y_2O_3 with lower valent cation dopants have concentrated on the use of CaO as an

additive[22,35]. Steele et al[35] used a Y_2O_3-CaO mixture designed to give an anion vacancy concentration of 1% (3 atomic % CaO). They determined that it was "immediately apparent from the variation of conductivity with the oxygen partial pressure and the associated E.M.F. values that at lower oxygen partial pressures the conduction mechanisms are all almost entirely ionic with an increasing contribution from p-type conductivity at the higher oxygen partial pressures" [35]. The authors were reluctant to speculate whether the ionic conductivity was due to the movement of cations or anions. In view of later work defining the self-diffusion coefficients[9,10] (Figure 1) it seems likely that anion movement was responsible for the ionic conductivity.

Etsell's[22] work with Y_2O_3-5%CaO showed similar results. Both p-type and ionic conductivity were observed, although the oxygen partial pressure dividing the ionic and mixed conductivity regions varied with temperature, from 10^{-10} atmospheres of oxygen at 600 C to 10^{-13} atmospheres of oxygen at 1100 C. The combined results of Steele and Etsell are shown in Figure 6.

C) Exsolution Phenomena in Oxides

Reaction kinetics involving the exsolution of a two-component oxide system have not been extensively researched. Only a few systems have drawn any attention. Stubican initiated the first general studies on grain boundary precipitation in oxide systems: ZrO_2-MgO [40] , and

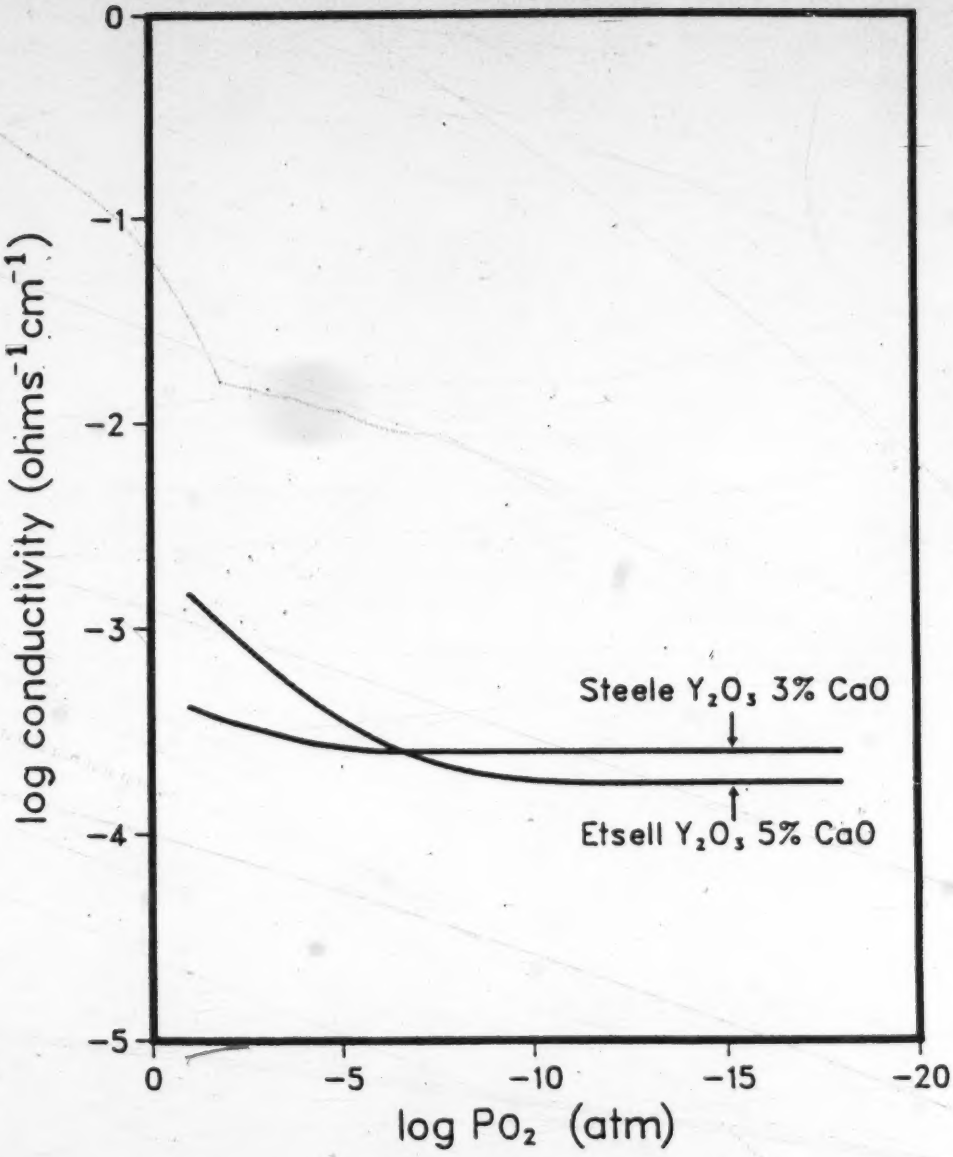

Figure 6. Conductivity data for Y_2O_3-CaO mixtures [33,35].

$MgO-Al_2O_3$ [41]. Subsequently, other researchers have studied the exsolution kinetics of oxide systems such as the $MgO-Sc_2O_3$ system [10], CaO-NiO system [42], and the $CaO-Yb_2O_3$ system[43].

Initial work by Stubican[40] involved the decomposition of a ZrO_2-MgO solid solution using samples prepared from a sol-gel process. The rate of decomposition from a cubic solid solution to a two phase mixture of tetragonal solid solution and pure MgO was followed using an x-ray diffraction technique.

The decomposition curves obtained were sigmoidal, indicating that the formation of the new phases began with a process of nucleation and growth. Accompanying electron microprobe studies showed that Mg ions diffused out of the grains and precipitated at the grain boundaries as MgO. It was also observed that the rate of decomposition generally increased as the concentration of the dopant ion (Mg^{2+}) increased, and was fastest when the initial concentration was equal to the solubility limit.

Similar findings were observed for $MgO-Al_2O_3$ [41]: the rate of precipitation was seen to increase with an increase in the amount of Al_2O_3 dissolved in solid solution with MgO. However, one significant difference between the two systems was observed. In $MgO-Al_2O_3$ there was no evidence to suggest the existence of an induction period similar to the one observed for the ZrO_2-MgO system.

A third system involving Yb_2O_3 and CaO has been

studied by Barry, Roy, and Stubican[43]. In this case the authors were concerned with the rate at which Yb_2O_3 would precipitate out of a CaO-Yb_2O_3 solid solution. Unfortunately, these data reflected structures at the alkaline earth oxide-rich end of the phase diagram, as opposed to the rare earth oxide-rich end, with which we were chiefly concerned. Nevertheless the results are generally applicable to other systems. Once again the exsolution rate increased as the concentration of cation vacancies increased. The concentration of cation vacancies was directly proportional to the concentration of the minor component (in this case Yb_2O_3).

Lopato examined the Sc_2O_3-MgO system[16] and suggested that such a system can be regarded as a model "to allow discussion of the general features of the decompostion of defect solid solutions involving oxides where the solid solutions decompose into the constituent components without the formation of a transition phase". Lopato's findings can be summarized as follows:

1) the decomposition of the solid solutions involved the precipitation of the minor component.

2) the degree of decomposition, at a given composition of the solid solution, increased with temperature.

3) an increase in the concentration of the dopant ion in the solid solution increased the rate of decomposition.

4) the distinctive feature of the exsolution rate, in

Sc_2O_3-MgO, was the lack of an induction period.

Lopato's work indicated that, at low temperatures (less than 1200 C), precipitation of Sc_2O_3 occurred at defects and not at grain boundaries. It was noted, however, that if the time of annealing was increased, then preferential precipitation of the Sc_2O_3 at the grain boundaries did occur.

The NiO-CaO system, studied by Smith et al[42], was of interest primarily because it provided an indication of the magnitude of the activation energy associated with exsolution. For CaO precipitating from a NiO rich solid solution, these authors found an activation energy of 196 kJ/mol.

Mathematical descriptions of the decomposition of solid systems have all taken the form $f(\alpha) = kt$, α being the fraction reacted, t the time, and k a characteristic rate constant. The form of the function is dependent on the reaction mechanism and the geometry of the reacting species.

Beretka[44] and Hancock and Sharp[45] proposed a series of nine equations (excluding the zero order case below) which can be applied to solid state reactions. They suggested an evaluation of each equation to determine which would best fit the experimental data. These equations (Table 2) can be subdivided into three groups: diffusion controlled reactions, phase boundary and first order reactions, and nucleation reactions.

Table 2. Solid state reaction rate equations.

Symbol	Model	Equations
0	Zero order	$\alpha = kt$
D1	One Dimensional Diffusion	$\alpha^2 = kt$
D2	Two Dimensional Diffusion	$(1-\alpha)\ln(1-\alpha)-\alpha = kt$
D3	Three Dimensional Diffusion	$(1-(1-\alpha)^{1/3})^2 = kt$
D4	Three Dimensional Diffusion	$(1-2/3\alpha)-(1-\alpha)^{1/3} = kt$
R2	Phase Boundary (disk)	$1-(1-\alpha)^{1/2} = kt$
R3	Phase Boundary (sphere)	$1-(1-\alpha)^{1/3} = kt$
A2	Nucleation (disk)	$-\ln(1-\alpha)^{1/2} = kt$
A3	Nucleation (sphere)	$-\ln(1-\alpha)^{1/3} = kt$
F1	First Order	$-\ln(1-\alpha) = kt$

III. THEORETICAL CONSIDERATIONS

A) Effects of Additives in Oxides

The addition of a second oxide to an oxide matrix (doping) affects the defect structure of the major component. It is, therefore, important to consider exactly what inherent defects exist in the starting material.

At one time, it was believed that inorganic compounds had an idealized unvarying structure; essentially a unit cell repeated itself over and over again. With time and improved investigation techniques, this idea gave way to the concept of nonstoichiometry; it was recognized that a defect-free crystal was the exception to the rule and could only be found under a limited range of conditions (usually temperature and the partial pressures of the components in the compound).

Once the concept of a defect-free crystal had fallen, it became apparent that, at any temperature, a compound could have any combination of several structural imperfections. These imperfections could take on any one of several forms but could be classified under one of the following headings:

1) Point Defects - the imperfection is limited to one structural or lattice site and its immediate vicinity.

2) Line Defects - the imperfection is characterized by displacements in the periodic structure along certain directions.

3) Plane Defects - the imperfections comprise stacking faults, grain boundaries, internal surfaces, and external surfaces.

To fully define the overall defect structure it is necessary to consider not only the structural defects, but also electronic imperfections, i.e. electrons and electron holes. These are all relatively free to move in the crystal. When the structural and electronic defects are characterized as a function of temperature and the partial pressure of the constituent atoms, we have a complete picture of the defect structure.

Because the two most common mechanisms of diffusion, vacancy and interstitial, involve point defects and because diffusion affects both the exsolution rate of the ceramic as well as the conductivity, further discussion will be restricted to point defects.

As a first step, let us review the types of point defects that can occur in an undoped sample. In order to study such defects in terms of defect reactions, it is necessary to have a system of notation. Although various authors have modified existing systems for their personal convenience, the widely accepted system defined by Kroeger and Vink[46] is employed throughout this thesis. Kroeger and Vink's notation uses the variables shown in Table 3.

In Table 3.the type of imperfection is denoted by a major symbol and the site the imperfection occupies is given by a subscript. A superscript is used to indicate the

Table 3. Kroger-Vink notation for describing crystal defects for a compound AB (where B is a non-metal).

Symbol	Type of Defect	Effective Charge
e'	quasi-free electron in the conduction band	-1
h'	quasi-free electron hole in the valence band	1
V^{x}_{A}	an A atom vacancy	0
V''_{A}	an ionized A atom vacancy	-2
V^{x}_{B}	an unionized B atom vacancy	0
A'_{B}	an A ion occupying a B atom site (A and B have different charges)	-1
B^{x}_{A}	a B atom occupying an A atom site (A and B have the same charge)	0
A_{i}	an A atom at an interstitial position	1
A^{x}_{A}	an A atom on an A site	0
B^{x}_{B}	a B atom on a B site	0
F^{x}_{A}	a foreign atom occupying an A atom site	0
V^{x}_{i}	An unoccuppied interstitial site	0

effective charge at that location. The effective charge is the charge on the site relative to the perfect crystal. Thus, when vacancies are present, all or part of the actual charge from the missing atom may also be missing.

The formation of an oxygen vacancy illustrates the application of this notation to defect reactions. The first step in the creation of an oxygen vacancy is the removal of

an oxygen atom from the crystal. This leaves two free electrons in the vicinity of the vacated lattice site, giving a "real" charge of -2. Since the "real" charge is unchanged, the effective charge will be 0. This step can be expressed by the following reaction, where the = sign means 'leads to' and is not as strict as a mathematical = sign.

$$O^{\times}_{o} = V^{\times}_{o} + 1/2\ O_2 \qquad \text{(Eq. 1)}$$

One or both of the free electrons can leave the immediate area (either by ionization or simply by conduction). If this occurs, the vacancy will become singly or doubly ionized. When electrons are removed, the vacancy is less negatively charged; that is its effective charge will increase by one or two depending on the degree of ionization. These situations are expressed by reactions (2) and (3):

$$V^{\times}_{o} = V^{\cdot}_{o} + e' \qquad \text{(Eq. 2)}$$

$$V^{\times}_{o} = V^{\cdot\cdot}_{o} + 2e' \qquad \text{(Eq. 3)}$$

As the equations show, an effective positive charge is represented by the superscript $^{\cdot}$, and an effective negative charge by $'$; an $^{\times}$ represents a neutral charge.

If a crystal is to obey the principle of electroneutrality, then the sum of all effective positive charges must be equal to the sum of all the effective negative charges. This principle is a basic condition in the treatment of defect equilibria and in the evaluation of

defect concentrations in crystals.

B) Defects in Stoichiometric Oxides

Perfectly stoichiometric oxide compounds are rare. Nevertheless, the chemical formula for oxides and other compounds as written usually indicate a specific cation to anion ratio. By taking advantage of modern experimental techniques, it is possible to measure the actual cation to anion ratio; and thus the assumption of stoichiometry implied by the chemical formula can be confirmed over a wide range of temperatures and partial oxygen pressures. Actual deviations from stoichiometry are often so small as to be negligible with regards to the chemical formula.

In a stoichiometric oxide, MO, when a positively charged point defect forms, in order to maintain electroneutrality a complimentary negatively charged point defect must also be formed. Kroeger outlined six basic types of defect structures which can exist in a stoichiometric compound. Of these six defect types, only two have been shown to be of significance in oxides. These defects are called Schottky and Frenkel defects and will be examined more closely.

A Schottky defect is a stoichiometric defect composed of a cation vacancy and an anion vacancy. Schottky disorders are a collection of Schottky defects. Such a disorder is shown schematically in Figure 7 for the example oxide (MO).

A Frenkel defect is a stoichiometric defect composed

of an ion in an interstitial site and its corresponding vacancy in the lattice. Frenkel disorders are a collection of Frenkel defects. Figure 8 gives a schematic representation of Frenkel disorder.

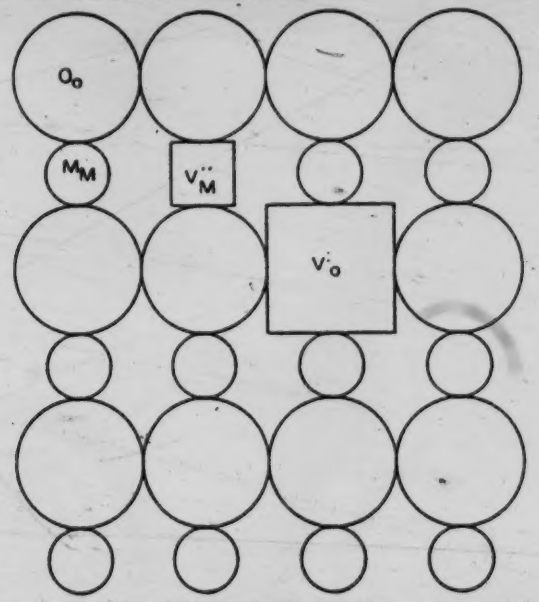

Figure 7. Schottky defect in an oxide MO.

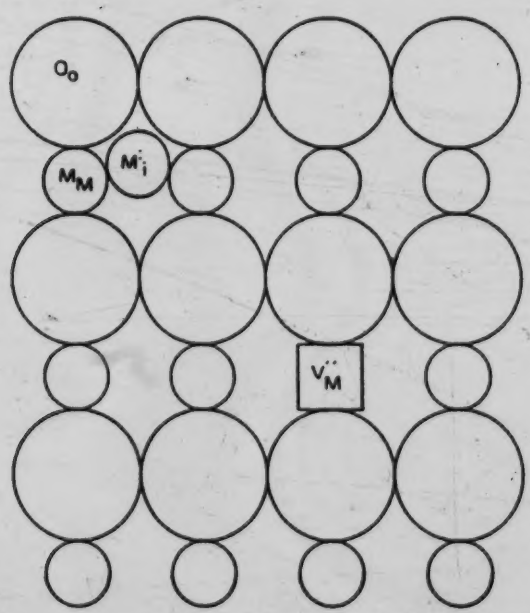

Figure 8. Frenkel defect in an oxide MO.

Although both types of disorder can be present in stoichiometric oxides, one form generally predominates. Schottky disorder usually predominates when the size of the cation and anion are similar; Frenkel disorder generally dominates when the cation and anion differ substantially in size.

Each of these disorders can be described using defect equations to represent the equilibrium situation. In order to fully understand the nature of the reactions, it is important to recognize the underlying principles used to develop them. The principle of electroneutrality has already been introduced. The second principle states that the ratio of cation to anion sites must be constant. Thus, in our oxide MO, the ratio of metal cation sites to oxygen anion sites is 1:1 regardless of the exact stoichiometry. The third principle states that the total number of regular sites may change in a defect reaction, as long as the second principle is still obeyed. The fourth and final principle states that defect reactions must obey the law of mass conservation.

With these principles in mind, we can look at the reactions associated with Schottky and Frenkel disorders. In Schottky disorder, where there are equal concentrations of metal and oxygen vacancies (oxide MO), the formation of a defect pair within the crystal involves the migration of a cation and anion pair from their regular lattice sites in the bulk of the crystal to the surface. If one starts with

a perfect lattice, the formation of Schottky disorder will result in the creation of two new lattice sites thus.

$$M^{\times}_{M} + O^{\times}_{O} = V''_{M} + V^{\cdot\cdot}_{O} + M^{\times}_{M} + O^{\times}_{O} \qquad \text{(Eq. 4)}$$

which can be reduced to

$$X = V''_{M} + V^{\cdot\cdot}_{O} \qquad \text{(Eq. 5)}$$

where X represents the perfect crystal.

In Frenkel disorder, the defect structure is limited to either cation or anion interstitials with corresponding vacancies. If we consider the situation where both the interstitial and the vacancy are doubly charged, then the defect reaction can be written as

$$M^{\times}_{M} = M^{\cdot\cdot}_{i} + V''_{M} \qquad \text{(Eq. 6)}$$

Thus, a metal ion on its normal site is transferred to an interstitial site and no new lattice sites are created.

Unfortunately, not all systems can be considered stoichiometric. Some, like wustite ($Fe_{1-y}O$), are not stable as a stoichiometric compound; others fail to be stoichiometric because more than one valence state is possible for the cation in the compound.

C) Defects in Nonstoichiometric Oxides

Nonstoichiometric oxides may be either oxygen ion deficient or metal ion deficient.

In the majority of cases, nonstoichiometric oxides are formed by reactions between the compound and the surrounding atmosphere: the type of defect that forms depends, in part, on the possible valence states of the metal ion. If the cation can exist in a lower valance state than the one it has in the oxide a V'_O defect usually develops; if the cation can exist in a higher valence, the result is commonly a V''_M defect.

Oxygen Deficient Oxides

Oxygen deficient oxide structures are dominated by either oxygen vacancies or interstitial metal ions.

Domination of oxygen vacancies is typified by a metal oxide system where the oxide is deficient in oxygen ions. The chemical formula of such an oxide can be expressed as MO_{2-x}.

Vacancy formation begins when the partial pressure of oxygen is sufficiently low so as to allow the net release of oxygen atoms: thus neutral vacancies are formed (they are neutral because the electrons remain in the "immediate vicinity"):

$$O^x_O = V^x_O + 1/2\ O_2 \qquad \text{(Eq. 7)}$$

In oxides where the cations are easily reduced (for example, ceria) there is a strong tendency towards

ionization of the neutral vacancies, especially at higher temperatures:

$$V^{x}_{o} = V^{\cdot}_{o} + e' \qquad \text{(Eq. 8)}$$

$$V^{\cdot}_{o} = V^{\cdot\cdot}_{o} + e' \qquad \text{(Eq. 9)}$$

where e' is a quasi-free electron which can reduce the cation:

$$e' + M^{x}_{M} = M'_{M} \qquad \text{(Eq. 10)}$$

The total formation reaction can be expressed as

$$O^{x}_{o} + 2\ M^{x}_{M} = V^{\cdot\cdot}_{o} + 2\ M'_{M} + 1/2\ O_2 \qquad \text{(Eq. 11)}$$

The oxygen vacancy and the reduced cation are of opposite charge and can, depending on the conditions, form defect clusters by electrostatic interactions, i.e.,

$$V^{\cdot\cdot}_{o} + M'_{M} = (V^{\cdot\cdot}_{o}M'_{M})^{\cdot} \qquad \text{(Eq. 12)}$$

Alternatively, oxygen deficient oxides may be dominated by interstitial metal ions. The interstitial ions occur with an equivalent number of electrons in the conduction band. This situation arises when an oxygen atom leaves a perfect MO crystal. The left over M^{2+} cation is then free to enter an interstitial site, while the oxygen ion electrons enter the conduction band. The formation of the defect can then be represented as

$$MO = M^{\cdot\cdot}_{i} + 2e' + 1/2\ O_2 \qquad \text{(Eq. 13)}$$

for doubly charged metal interstitials, and as

$$MO = M^{\cdot}_{i} + e' + 1/2\ O_2 \qquad \text{(Eq. 14)}$$

for singly charged interstitial metal ions.

Metal Deficient Oxides

Metal deficient oxides can have either metal vacancies or interstitial oxygen ions as the dominant defect.

The formation of a metal vacancy involves four steps. First, oxygen is adsorbed onto the crystal surface where it dissociates:

$$1/2\ O_2 = O_{(ad)} \qquad \text{(Eq. 15)}$$

Electrons from two cations adjacent to the new oxygen site join the adsorbed oxygen to form an oxygen ion.

$$O_{(ad)} = O^- + h^{\cdot} \qquad \text{(Eq.16)}$$

In order to maintain the cation to anion ratio (principle 2), surface metal vacancies must be formed:

$$O^- = O^{x}_{O} + V^{''}_{M} + h^{\cdot} \qquad \text{(Eq. 17)}$$

The final step begins with the diffusion of cations from the interior of the crystal to the surface. The holes formed in the previous steps can react with the cations to form a positively charged cation site:

$$h^{\cdot} + M^{x}_{M} = M^{\cdot}_{M} \qquad \text{(Eq. 18)}$$

Thus, the overall reaction is

$$1/2\ O_2 + 2M^x_M = V''_M + 2\ M^{\cdot}_M + O^x_O \quad \text{(Eq. 19)}$$

Singly charged and neutral vacancies are very unlikely, since such a situation would require 1 or 2 electrons to be stabilized in a cation lattice position. The defects discussed above are much more likely to form the following defect clusters: $(V''_M 2M^{\cdot}_M)$ and $(V''_M M^{\cdot}_M)'$.

The second possibility for metal deficient oxides involves the rarely observed oxygen interstitials. The formation of the interstitial oxygen ion begins when an oxygen atom is absorbed into a relatively open oxide lattice (UO_2 for example):

$$1/2\ O_2 = O''_i + 2h^{\cdot} \quad \text{(Eq. 20)}$$

$$2\ M^x_M + 2\ h^{\cdot} = 2M^{\cdot}_M \quad \text{(Eq. 21)}$$

The overall reaction is

$$1/2\ O_2 + 2\ M^x_M = O''_i + 2M^{\cdot}_M \quad \text{(Eq. 22)}$$

indicating that the metal ion is oxidized.

Intrinsic Ionization

Electronic defects, quasi-free electrons and electron holes, can also be formed by a "spontaneous" reaction. This process, which predominates when the concentration of other defects is extremely small, is expressed as:

$$X = e' + h^{\cdot} \quad \text{(Eq. 23)}$$

D) The Effects of Doping on Defect Structure

Aliovalent doping of oxides will significantly affect the defect concentration. Substitutional defects occur in the host lattice when a cation is replaced by a dopant cation. The type of defect depends on the valence of the substituting ion relative to the original ion. There are three possible situations:

1) the valence of the dopant ion is lower than that of the original cation: oxygen vacancies are formed to maintain electrical neutrality.

2) the valence of the dopant ion is the same as the original system: no point defects are introduced.

3) the valence of the dopant ion is higher than that of the original cation: oxygen interstitials are formed to maintain electrical neutrality.

Calculating the Defect Concentration

The "site fraction" of a given point defect can be related to the deviation from stoichiometry using the following notation:

n_o^t - the total number of lattice oxygen sites

n_M^t - the total number of lattice metal sites

n_v° - the number of oxygen vacancies

n_i° - the number of oxygen interstials

n_v'' - the number of metal vacancies

n_i'' - the number of metal interstitials

In an oxygen deficient oxide with the composition

MO_{2-x}, the actual oxygen to metal ion ratio will be given by:

$$\frac{O}{M} = 2-x = \frac{(n_o^{\bullet} - n_v^{\circ})}{n_M^{\bullet}} \qquad \text{(Eq. 24)}$$

The relationship between the total number of oxygen lattice sites and the total number of metal lattice sites is given by "ideal" stoichiometry as:

$$n_M^{\bullet} = 1/2\ n_o^{\bullet} \qquad \text{(Eq. 25)}$$

Substituting for $n_M^{\bullet}$ in equation (24) then:

$$2-x = 2(n_o^{\bullet} - n_v^{\circ})/n_o^{\bullet}$$

$$= 2(1-(n_v^{\circ}/n_o^{\bullet})) \qquad \text{(Eq. 26)}$$

which can be rearranged to give:

$$\frac{n_v^{\circ}}{n_o^{\bullet}} = \frac{x}{2} \qquad \text{(Eq. 27)}$$

where $n_v^{\circ}/n_o^{\bullet}$ is the concentration of oxygen vacancies, $[\ V_O^{\bullet\bullet}\ ]$.

Similarly, for metal deficient oxides ($M_{1-x}O$), oxygen excess oxides (MO_{2+x}), and metal excess compounds ($M_{1+x}O$) the respective defect concentrations are $[\ V_M^{''}\ ] = x$, $[\ O_i^{''}\ ] = x/2$, and $[\ M_i^{\bullet}\ ] = x$.

Simple Defect Equilibria

At sufficiently low defect concentrations, an oxide is assumed to behave like an ideal solution, ($\gamma_{defect} = 1$), and consequently obeys Henry's law:

$$a_{defect} = \gamma_A [defect] \qquad \text{(Eq. 28)}$$

where γ_A is the activity coefficient of the defect in the solid solution. Other assumptions useful for determining the defect equilibria are the following:

1) the defects are randomly distributed.
2) the energy associated with defect formation is constant and independent of defect concentration.
3) the interactions between defects are negligible.
4) the defects are highly mobile.
5) the concentrations of the lattice atoms in their normal sites are relatively large and approximately constant and can therefore be set at unity.

For an oxygen deficient oxide, the following analysis of the defect equilibrium can be performed. The overall defect equilibria for an oxide MO_2 is

$$O^x_o + 2M^x_M = V^{\cdot\cdot}_o + 2\,M^{\cdot}_M + 1/2\,O_2 \qquad \text{(Eq. 11)}$$

The equilibrium constant for this reaction will be

$$K_{eq} = \frac{a(V^{\cdot\cdot}_o)a(M^{\cdot}_M)^2 a(O_2)^{1/2}}{a(O^x_o)a(M^x_M)^2} \qquad \text{(Eq. 29)}$$

The denominator of equation (29) is equal to one (assumption 5). Since the system is assumed to be ideal, the activities of the species in the numerator can be replaced by their relative concentrations. So the numerator can be approximated by $[V^{\cdot\cdot}_O][M^{\cdot}_M]^2 P_{O_2}^{1/2}$ so, equation (29) is simplified:

$$K_{eq} = [V^{\cdot}_{O}][M'_{M}]^{2}Po_{2}^{1/2} \qquad \text{(Eq. 30)}$$

In the stoichiometry of equation (11), two reduced cations are formed for each oxygen vacancy, so

$$2[V^{\cdot}_{O}] = [M'_{M}] \qquad \text{(Eq. 31)}$$

Substituting for $[M'_{M}]$ in equation (30):

$$K_{eq} = 4[V^{\cdot}_{O}]^{2}Po_{2}^{1/2} \qquad \text{(Eq. 32)}$$

By rearranging equation equation (32):

$$[V^{\cdot}_{O}] = (K_{eq}/4)^{1/3}Po_{2}^{-1/6} \qquad \text{(Eq. 33)}$$

Hence,

$$[V^{\cdot}_{O}] \propto Po_{2}^{-1/6} \qquad \text{(Eq. 34)}$$

Thus, a plot of the log of the vacancy concentration against the log of the partial oxygen pressure (a so called Brouwer diagram) should give a straight line with a slope of -1/6. Similar analyses can be applied to metal deficient oxides and to excess oxygen oxides to demonstrate that

$$[V^{\cdot}_{M}] \propto Po_{2}^{1/6} \qquad \text{(Eq. 35)}$$

$$[O''_{i}] \propto Po_{2}^{1/6} \qquad \text{(Eq. 36)}$$

Complex Defect Equilibria

In many cases where the cation is multivalent, the nature of the defect can change with the partial pressure of oxygen. This makes the analysis of the defect equilibria more complicated. For example, if a metal can exist in lower or higher valence states than normally exist in the oxide of interest, then the oxide can be an oxygen deficient system (MO_{2-x}) or an oxygen excess system (MO_{2+x}), respectively. In order to understand the defect equilibria, we must consider the following four defect reactions and their equilibria.

1) Formation of oxygen vacancies:

$$O^x_o = V^{\cdot\cdot}_o + 2e' + 1/2\ O_2 \qquad \text{(Eq. 37)}$$

$$K_v = [V^{\cdot\cdot}_o]n^2 P_{O_2}^{1/2} \qquad \text{(Eq. 38)}$$

where n represents the electron concentration.

2) Formation of oxygen interstitials:

$$1/2\ O_2 = O''_i + 2h^{\cdot} \qquad \text{(Eq. 39)}$$

$$K_i = [O''_i]p^2 P_{O_2}^{-1/2} \qquad \text{(Eq. 40)}$$

where p is the electron hole concentration

3) Intrinsic ionization

$$X = e' + h^{\cdot} \qquad \text{(Eq. 41)}$$

$$K_i = np \qquad \text{(Eq. 42)}$$

4) Formation of anti-Frenkel disorder

$$O^{x}_{o} = V^{\cdot}_{o} + O^{\cdot\cdot}_{i} \qquad \text{(Eq. 43)}$$

$$K_F = [V^{\cdot}_{o}][O^{\cdot\cdot}_{i}] \qquad \text{(Eq. 44)}$$

The principle of electroneutrality must also be obeyed. From equation (37), we see that

$$2[V^{\cdot}_{o}] = n \qquad \text{(Eq. 45)}$$

and from equation (39) we see that

$$2[O^{\cdot\cdot}_{i}] = p \qquad \text{(Eq. 46)}$$

and for neutrality to be maintained:

$$2[O^{\cdot\cdot}_{i}] + n = 2[V^{\cdot}_{o}] + p \qquad \text{(Eq. 47)}$$

This series of equations can be solved directly to establish the relationship between the defect concentration and the oxygen partial pressure. Alternatively, we can make the additional simplifying assumption that only one term on each side of the neutrality equation will be significant.

In the situations where the partial pressure of oxygen is low, equation (37) will dominate. Thus the concentration of oxygen vacancies will be much greater than that of oxygen interstitials and n will be much greater than p. The neutrality equation becomes:

$$n = 2[V^{\cdot}_{o}] \qquad \text{(Eq. 48)}$$

Substituting this into equation (38) and rearranging to find the oxygen vacancy concentration:

$$[V'_o] = (K_v/4)^{1/3} P_{O_2}^{-1/6} \qquad \text{(Eq. 33)}$$

and substituting equation (33) into equation (48):

$$n = (2K_v)^{1/3} P_{O_2}^{-1/6} \qquad \text{(Eq. 49)}$$

Substituting equation (49) into the equilibrium equation for intrinsic ionization. equation (42), and solving for p:

$$p = \frac{K_i}{n} = K_i (2K_v)^{-1/3} P_{O_2}^{1/6} \qquad \text{(Eq. 50)}$$

Rearranging (44):

$$[O''_i] = K_F / [V'_o] \qquad \text{(Eq. 51)}$$

and substituting equation (33) into equation (51), the dependence of the interstitial concentration on the oxygen partial pressure is seen to be:

$$[O''_i] = K_F (K_v/4)^{-1/3} P_{O_2}^{+1/6} \qquad \text{(Eq. 52)}$$

When the oxygen partial pressure is in an intermediate range, we must consider two cases. In the first case, where there is a low defect concentration, intrinsic ionization becomes important. This situation is described by the following reactions:

$$n = p = K_i^{1/2} \qquad \text{(Eq. 53)}$$

$$[O''_i] = (K_I/K_i) P_{O_2}^{1/2} \qquad \text{(Eq. 54)}$$

$$[V'_o] = (K_v/K_i] P_{O_2}^{-1/2} \qquad \text{(Eq. 55)}$$

The above equations are derived from equations 42. 40

and 53. and 38 and 53 respectively.

In the second case, the formation of anti-Frenkel disorders is significant and the equations are:

$$[O''_i] = [V^{\cdot}_o] = K_F^{1/2} \qquad \text{(Eq. 56)}$$

$$n = K_v^{1/2} K_F^{-1/4} P_{O_2}^{-1/4} \qquad \text{(Eq. 57)}$$

$$p = K_I^{1/2} K_F^{-1/4} P_{O_2}^{1/4} \qquad \text{(Eq. 58)}$$

The above equations are derived from equations 44, 38 and 56, and 40 and 56 respectively.

When the partial pressure of oxygen is high, oxygen interstitials will be the predominant defect and the neutrality condition is,

$$p = 2[O''_i] \qquad \text{(Eq. 59)}$$

In this situation, the concentration of the defects are described by the following set of equations:

$$[O''_i] = (K_I/4)^{1/3} P_{O_2}^{1/6} \qquad \text{(Eq. 60)}$$

$$[V^{\cdot}_o] = K_F (K_I/4)^{-1/3} P_{O_2}^{-1/6} \qquad \text{(Eq. 61)}$$

$$p = (2K_I)^{1/3} P_{O_2}^{1/6} \qquad \text{(Eq. 62)}$$

$$n = K_i (2K_I)^{-1/3} P_{O_2}^{-1/6} \qquad \text{(Eq. 63)}$$

The above equation are derived from equations 40 and 59, 44 and 60, 40 and 59, 42 and 62 respectively.

Defect Structure and Electrical Conductivity

Small changes in stoichiometry can significantly alter the electrical conductivity of a compound. Because of the relationship between nonstoichiometry and point defects,

studying the effects upon the electrical conductivity of oxygen partial pressure and temperature can give important information about the defect structure.

Most oxides are electronic conductors under the right conditions. This indicates the presence of mobile electrons and electron holes within the oxide. Because these defects can be highly mobile, they do not have to be the dominant defect to significantly affect conductivity. However, when electrons or electron holes dominate, the oxide can be classified as an "n" or "p" type conductor, respectively. Under special conditions of oxygen partial pressure and temperature, the oxide may be either a mixed conductor or a predominately ionic conductor. Ionic conduction will dominate in those oxides in which the concentration of electronic defects is much lower than the vacancy concentration. Thus, doping with lower valent cations, leads to the creation of vacancies and enhances the ionic conductivity. Equation (64) represents the generation of the substitutional defects that occur with the addition of a lower valent foreign atom:

$$2\,FO = 2F'_M + V'_O + O_2 \qquad \text{(Eq. 64)}$$

In this situation the electroneutrality equation becomes

$$[V'_O] = 1/2[F'_M] \qquad \text{(Eq. 65)}$$

The relationship between conductivity and the defect

structure can give an indication of the conductivity behaviour under varying oxygen partial pressures.

The total electrical conductivity (σ_t) is the sum of the ionic conductivity (cations or anions being the charge carriers) and the electronic conductivity (electrons or electron holes being the charge carriers).

$$\sigma_t = \sigma_i + \sigma_e = \sigma_C + \sigma_A + \sigma_n + \sigma_p \qquad \text{(Eq. 66)}$$

where σ_i is the ionic conductivity, σ_e is the electronic conductivity, and σ_C, σ_A, σ_n, σ_p are the conductivities due to cations, anions, electrons, and electron holes respectively. The conductivity can then be defined as

$$\sigma_j = q_j c_j \mu_j \qquad \text{(Eq. 67)}$$

where q_j is the charge on a carrier, c_j is the concentration of the charge carrier and μ is the carrier mobility (velocity per unit electric field).

For an oxygen deficient oxide (MO_{1-x}) where oxygen vacancies and electrons are the dominant defects, equation (66) becomes

$$\sigma_t = \sigma_A + \sigma_n \qquad \text{(Eq. 68)}$$

Using equation (67) to substitute for σ_A and σ_n, this becomes

$$\sigma_t = q_A c_A \mu_A + q_n c_n \mu_n \qquad \text{(Eq. 69)}$$

and since A is V'_o and e is the charge on an electron

$$\sigma_i = 2e[V'_o]\mu_{V'_o} + en\mu_n \qquad \text{(Eq. 70)}$$

But from equations (48) and (49) we have

$$n = 2[V'_o] = (2K_v)^{1/3}P_{O_2}^{-1/6} \qquad \text{(Eqs. 48 and 49)}$$

If we have predominately ionic conduction, the second term of equation (68) becomes negligible; therefore

$$\sigma_i = e(2K_v)^{1/3}P_{O_2}^{-1/6}\mu_{V'_o} \qquad \text{(Eq. 71)}$$

In this way, we can predict that the ionic conductivity should be proportional to $P_{O_2}^{-1/6}$. It is not possible however, to identify the predominate type of defect based on conductivity measurements alone. A metal-excess solid oxide will have the same relationship with the oxygen partial pressure as the oxygen-deficient solid oxide discussed here.

When equation (65) replaces the previous neutality expression, equation (48), the dependence of the conductivity on the oxygen partial pressure is lost.

F) Decomposition of Solids

The majority of phase transformations that occur in the solid state require thermally activated atomic motion. If we consider the situation where a change in temperature causes the shift from a single phase region of a binary phase diagram to a two phase region, the following transformations are possible:

1) precipitation transformation.

2) eutectoid transformation.

3) ordering reaction.

4) massive transformation.

5) polymorphic transformation.

The precipitation transformation, which is the one important to this work, is the exsolution of two phases from an initial single phase region. Such a transformation can be described by the following reaction:

$$\alpha' = \alpha + \beta \qquad \text{(Eq. 72)}$$

where α' is a metastable supersaturated solid solution, α is a more stable solid solution closer to equilibrium and β is a relatively stable precipitate. In general, the precipitation reaction (and the other transformations) will take place by nucleation and growth.

Heterogeneous Nucleation

Nucleation in solids is almost always heterogeneous. Suitable nucleation sites are non-equilibrium defects such as excess vacancies, dislocations, grain boundaries, stacking faults, inclusions and free surfaces. As we have seen, the precipitation of a second phase at the grain boundaries is the most common mode of exsolution in oxides.

The free energy of formation associated with the creation of a nucleus can be described by[47]

$$\Delta G_{het} = -V(\Delta G_v - \Delta G_s) + A\gamma - \Delta G_d \qquad \text{(Eq. 73)}$$

where V is the volume of the precipitate, G_v is the volume free energy change associated with the creation of the stable precipitate phase, G_s is the misfit strain energy, $A\gamma$ is the free energy increase associated with the creation of an interface, and G_d is the free energy change associated with the destruction of an interface.

Ignoring any misfit strain energy, (G_s), the optimum nucleus will be the one that has the lowest value of $A\gamma$. As a result, the optimum shape for an incoherent grain boundary nucleus will be two abutted spherical caps as shown in Figure 9.[47]

The angle θ, in Figure 9, will be given by

$$\cos\theta = \gamma_{\alpha\alpha} / 2\gamma_{\alpha\beta} \qquad \text{(Eq. 74)}$$

and the excess free energy can be described by

$$\Delta G = -V\Delta G_v + A_{\alpha\beta}\gamma_{\alpha\beta} - A_{\alpha\alpha}\gamma_{\alpha\alpha} \qquad \text{(Eq. 75)}$$

where V is the volume of the nucleus, $A_{\alpha\beta}$ is the area of the α/β interface of energy $\gamma_{\alpha\beta}$ created, and $A_{\alpha\alpha}$ is the area of the α/α grain boundary of energy $\gamma_{\alpha\alpha}$ destroyed during the process.

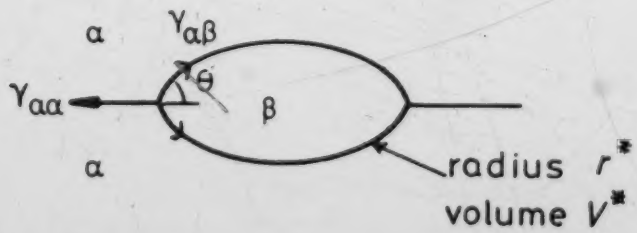

Figure 9. The critical nucleus size for grain boundary nucleation.[47]

Nucleation Kinetics

Many mathematical models have been formulated to relate nucleation and grain growth to the kinetics of phase transformations and decomposition. The growth of spherical precipitates from a solid solution was first analyzed in 1949 by Zener[48]. Since then, other models have been proposed ranging from the idealized approach of Schmalzried[49] to the generalized analysis of Ziabicki[50-53]. Other models have been proposed by Avrami[54], Erofe'ev[55], Fine[56] and Christian[57]. The following is an extension of Christian's ideas as proposed by Hulbert[58].

If we consider the precipitation reaction (equation 72) where the precipitate is growing from randomly distributed nuclei within the primary phase, then at time t the unreacted volume of phase α' is V'. Between t_o and $t_o + dt$ a number of new nuclei are formed. The number of new nuclei formed will be given by $IV'dt$ where I is the nucleation rate per unit volume.

At this point, Hulbert uses the assumption that precipitate growth will be isotropic (i.e., spherical). As we have already seen this is a reasonable assumption for oxide systems. Therefore, when the growth of nuclei is diffusion controlled the growth rate in any direction should be proportional to $(Dt)^{0.5}$ where D is the diameter of the spherical precipitate.

The volume of α' that has undergone the precipitation reaction after time t is designated by R and is given by

$$R = (4/3)\pi D^{1.5}(t-t_o)^{1.5} \qquad \text{(Eq. 76)}$$

During the initial stages of the reaction (when V^c, the volume consumed between times t and t+dt, is much less than the unreacted volume, V'), the nuclei are widely spaced and there is no competition between growing nuclei for space. In this case, the volume of α' that has decomposed is

$$dV^c = RIV'dt \qquad \text{(Eq. 77)}$$

Since V' is effectively constant and approximately equal to the original volume, V, the total volume of α' that has undergone the precipitation reaction at any time t, is given by:

$$V^c = (4/3)\pi V\int_{t_0}^{t} ID^{1.5}(t-t_o)^{1.5}dt \qquad \text{(Eq. 78)}$$

If I is assumed constant then equation (78) becomes

$$V^c = (8/15)\pi VID^{1.5}t^{2.5} \qquad \text{(Eq. 79)}$$

If we now let α represent the fraction of the original phase reacted, we find

$$\alpha = V^c/V = (8/15)\pi ID^{1.5}t^{2.5} \qquad \text{(Eq. 80)}$$

As the number of nuclei increases, it becomes progressively less likely that the nuclei will be able to grow unimpeded. In this case the nuclei continue to grow, except along the interface where two nuclei meet.

During the time dt, when IV'dt new transformed regions

are nucleated, a certain amount of nuclei would have formed in the reacted area had some product not already been formed there. These regions have been called "phantom nuclei" by Avrami[64] and have an associated "extended" volume of consumed reactant V^c_e, defined by

$$dV^c_e = RI\,(V' + V)^c\,dt \qquad \text{(Eq. 81)}$$

or

$$V^c_e = (4/3)\pi V \int_{t_o}^{t} ID^{1.5}(t-t_e)^{1.5}dt \qquad \text{(Eq. 82)}$$

The extended volume differs from the actual volume of reactant in two ways: it includes the phantom nuclei and it treats all regions as single entities unaffected by other regions. The extended volume is simply related to the kinetic laws of growth. The problem of impingement is resolved once a relationship between V^c_e and V^c is found. This is done by considering a small region, of which a fraction $(1- V^c/V)$, where V is the original volume, remains unreacted. During a time element dt, the extended volume of reactant converted will increase by dV^c_e and the actual volume converted will increase by dV^c. Part of the extended volume will be in previously reacted material. A fraction $(1-V^c/V)$ will lie in unreacted material and contribute to dV^c. The remaining fraction will be in already reacted material and contributes to dV^c_e. The relationship between V^c and V^c_e is given as

$$dV^c = (1 - V^c/V)dV^c_e \qquad \text{(Eq. 83)}$$

or

$$V^c_o = -V\ln(1-V^c/V) \qquad \text{(Eq. 84)}$$

If we substitute this equation into equation (82)

$$-\ln(1-\alpha) = (4/3)\pi\int_{t_o}^{t} ID^{1.5}(t-t_o)^{1.5}dt \qquad \text{(Eq. 85)}$$

When I is constant, then integration of equation (85) yields

$$\ln \frac{1}{1-\alpha} = kt^{2.5} \qquad \text{(Eq. 86)}$$

The analysis is based on the assumption that nucleation is random. It does not preclude the possibility that nuclei may form preferentially at certain sites. only that these active sites be randomly distributed.

The nucleation rate, I, is in fact rarely constant. It can either increase or decrease; the number of active sites remaining at any time is given by

$$N_t = N_o\exp[\ -ft\ ] \qquad \text{(Eq. 87)}$$

where N_o is the initial number of preferred nucleation sites and f is the nucleation frequency of the sites. The nucleation rate, I, is

$$I = fN_t = fN_o\exp[\ -ft\ ] \qquad \text{(Eq. 88)}$$

When ft is small, then I is effectively constant and equal to fN_o. If we substitute this relationship into equation (85), then integrate and rearrange the result:

$$\ln \frac{1}{1-\alpha} = \frac{8\pi}{15} fN_o D^{1.5} t^{3.5} \qquad \text{(Eq. 89)}$$

In the case where ft is very large, the nucleation occurs so rapidly that the nucleation time may be considered as 0. That is, N_s quickly becomes 0 indicating that all nucleation sites are quickly exhausted. The volume of the α' phase which transformed to $\alpha + \beta$ initially is given by:

$$R = (4/3)\pi \; D^{1.5} t^{1.5} \qquad \text{(Eq. 90)}$$

At time t, the extended volume of the α' phase, V^c_o, will be the product of the number of nuclei present, N_o, and the volume of an individual nuclei, R_s:

$$V^c_o = RN_o = N_o \; 4/3\pi \; D^{1.5} t^{1.5} \qquad \text{(Eq. 91)}$$

Using the established relationship between V^c_o and V^c:

$$\ln \frac{1}{1-\alpha} = kt^{1.5} \qquad \text{(Eq. 92)}$$

In the event that the growth of nuclei is phase-boundary controlled, then the growth rate, G, is proportional to time and the volume of the reactant precipitated by time t will be

$$R = (4/3)\pi \; G^3 (t - t_o)^3 \qquad \text{(Eq. 93)}$$

If this relationship is substituted into the equation for the extended volume then:

$$\ln(1/(1-\alpha)) = (4/3)\pi G^3 \int_{t_o}^{t} I(t-t_\bullet)^3 dt \qquad \text{(Eq. 94)}$$

By holding the nucleation rate (I) constant and integrating the above reaction:

$$\ln \frac{1}{1-\alpha} = (\pi/3)G^3 I t^4 \qquad \text{(Eq. 95)}$$

If all the nuclei were present at the start of the reaction, then the extended volume of the reactant consumed at time t is

$$V^c_\bullet = RN_\bullet = (4/3)\pi\, N_\bullet G^3 t^3 \qquad \text{(Eq. 96)}$$

and by combining with equation (84):

$$\ln (1/(1-\alpha)) = N_\bullet (4/3)\pi G^3 t^3 \qquad \text{(Eq. 97)}$$

Equations for the one and two dimensional growth cases can be developed for both diffusion and phase boundary controlled situations. In all cases, the nuclei growth equations have the general form:

$$\ln(1/(1-\alpha)) = kt^m \qquad \text{(Eq. 98)}$$

where m a function of the reaction mechanism, the nucleation rate, and the geometry of the nuclei. Table 4 summarizes the value of m which may be obtained for various boundary conditions.

On the basis of this theory, a solid-solid reaction can be represented by a nucleation and growth model wherein a plot of ln ln(1/(1-α) vs ln t yields a straight line with

a slope m and an intecept ln k.

Table 4. Values of m for nuclei growth models for solid-solid interactions.[58]

	Phase Boundary Controlled	Diffusion Controlled
Three-Dimensional Growth		
Constant Nucleation Rate	4.0	2.5
Zero Nucleation Rate	3.0	1.5
Decreasing Nucleation Rate	3.0-4.0	1.5-2.5
Two-Dimensional Growth		
Constant Nucleation Rate	3.0	2.0
Zero Nucleation Rate	2.0	1.0
Decreasing Nucleation Rate	2.0-3.0	1.0-2.0
One-Dimensional Growth		
Constant Nucleation Rate	2.0	1.5
Zero Nucleation Rate	1.0	0.5
Decreasing Nucleation Rate	1.0-2.0	0.5-1.5

IV EXPERIMENTAL

While yttria is a stable compound and has shown some ionic conductivity, there was no guarantee that the yttria-calcia system would retain the stability of pure yttria. The ionic conductivity of yttria-calcia appeared to be better than pure yttria but the kinetics of exsolution would certainly affect the stability of the ternary material.

To study these effects, the Y_2O_3 and CaO were mixed together using a coprecipitation technique. This ensured a homogeneous mixture on a fine particle scale and perhaps on an atomic level.

After the powder preparation technique had been established, the degree of solid solubility and the exsolution kinetics were determined by x-ray diffraction. Finally, the conductivity characteristics were determined.

A) Sample Preparation

The yttria-calcia mixtures were prepared using an oxalate co-precipitation technique (Figure 10). For the phase and kinetic studies, 99.99% Y_2O_3 and 100.0% $CaCO_3$ were dissolved in 200 ml of hot distilled water containing 40% excess 10 M nitric acid. The analyses of the starting materials are shown in Table 5.

The acidic solution was neutralized with 7.5 M ammonium hydroxide; bromothymol blue was used as an

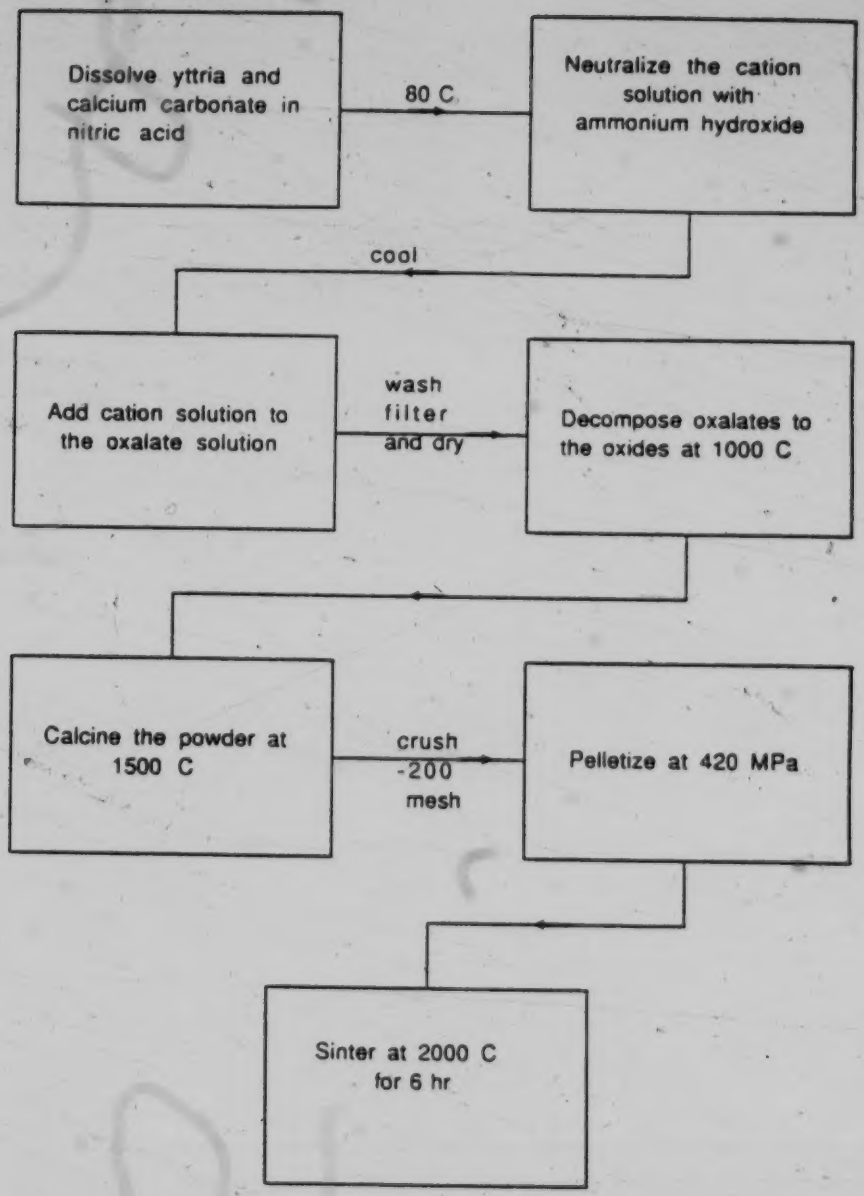
Dissolve yttria and calcium carbonate in nitric acid
80 C
Neutralize the cation solution with ammonium hydroxide
cool
Add cation solution to the oxalate solution
wash filter and dry
Decompose oxalates to the oxides at 1000 C
Calcine the powder at 1500 C
crush -200 mesh
Pelletize at 420 MPa
Sinter at 2000 C for 6 hr

Figure 10. The coprecipitation flowsheet.

indicator. Following the neutralization step, the solution was allowed to cool to room temperature. During this time, 300 ml of an ammonium oxalate solution was prepared using 150% of the theoretical amount of oxalate required for complete precipitation. The cation solution was then added to the oxalate solution in a so-called "reverse strike". The resulting precipitate was fine grained and settled quite slowly. The precipitate was filtered immediately to prevent segregation. The addition of more oxalate to the filtrate ensured that all the Y^{3+} and Ca^{2+} ions had precipitated, any additional precipitate was treated in an identical manner to the original precipitate. After washing with distilled water and drying in an oven at 108 C, the residue was transferred to a porcelain crucible and decomposed at 1000 C.

Table 5. Impurities in Y_2O_3 and $CaCO_3$.

Impurity	Y_2O_3 (ppm)	Impurity	$CaCO_3$ (ppm)
Si	70	Sr	300
Ca	20	Na	100
Ce	20	$SO_4^=$	<100
Gd	7	Ba	< 50
Fe	.5	NH_4	30
Dy	.5	Fe	< 20
		Mg	< 20
		K	< 1

The powder was then calcined in a platinum crucible at 1500 C for 48 hours and subsequently ground to -200 mesh. The powder was then compacted at 420 MPa in a tool steel die. The resulting pellets were 1.27 cm in diameter and

0.25 to 0.35 cm thick.

Subsequent analysis indicated that the oxalate precipitation method consistently produced a powder that was within plus or minus 4% (by weight) of the expected composition.

The pellets were sintered at 2000 C for 6 hr in a Brew vacuum furnace. Futher sintering did not change either the peak height or peak location on an x-ray powder diffraction pattern indicating that equilibrium between Y_2O_3 and CaO had been reached after 6 hr. The pellets were surrounded by a matrix powder of identical composition and supported in either a calcia-stabilized zirconia (CSZ) crucible or between two CSZ setter plates. Following sintering, the pellets had a black appearance as a result of carbon (from the graphite furnace refractories) depositing on their surface. A ten minute anneal in air at 1200 C removed the carbon and returned the pellets to their characteristic off-white colour.

B) Phase Study

The degree of solid solubility was determined using a Phillips x-ray diffractometer. An x-ray technique was used to determine the lattice parameter of the Y_2O_3-CaO mixtures which, according to Vegard's law[59], was proportional to the atomic percent of the dissolved solute (CaO in this case). As the amount of CaO dissolved in Y_2O_3 increased, the lattice parameter of Y_2O_3 increased due to replacement of the Y^{3+} ion (0.92 A) in the crystal structure by the larger

Ca^{2+} (0.99 A). When the solubility limit was reached, the lattice parameter of the solid solution remained constant and the presence of CaO was detected by the diffractometer.

The degree of solid solution was determined at 1200, 1400, 1600, 1800, and 2000 C using a parametric method[**]. Pellets of compositions: 0, 1, 2, 5, 7, 10, 15, 20, and 25% CaO were sintered at 2000 C as previously described. The pellets were then cooled down to the required temperatures and allowed to equilibrate (6 hr at 1800 C and 48 hr at 1200 C). After equilibrium had been reached, the samples were quenched by continuous argon flushing. This allowed the system to cool from 2000 C to 1000 C within five minutes. Below 1000 C the cooling rate slowed, but because of the extremely small diffusion coefficients at these lower temperatures, the extra cooling time did not have a significant effect.

Following the oxidizing anneal, the pellets were crushed in a Diamonite mortar to -200 mesh and placed in the x-ray diffractometer. The resulting x-ray pattern was used to calculate the lattice parameter. The lattice parameter was plotted against the molar percent of CaO to determine the solid solubility at each specific temperature.

C) Kinetics of Exsolution

The kinetic study involved only Y_2O_3-10%CaO pellets prepared in an identical manner to the phase study. At 2000 C, all of the CaO enters into solid solution.

The samples were quenched from 2000 C to room temperature and then reheated to the required temperature (1200-1800 C). The reheating procedure took between 10 and 15 min. The sample was held at a constant temperature over a range of reaction times from 1/2 hr to 48 hr, with time zero being the time at which the furnace reached the required temperature.

Upon completion of the reheat cycle the sample was given an oxidizing anneal and the lattice parameter was measured. The amount of CaO remaining in solid solution was determined by comparing the observed lattice parameter with the lattice parameter of prepared standards. Thus a plot of the lattice parameter versus time could be converted to one of "fraction reacted" $f(\alpha)$ versus time where 0% reacted represented the saturated solid solution state and 100% reacted, the equilibrium state at the required temperature.

The rate equations of Table 2 (page 24) were then compared, using plots of $f(\alpha)$ against time, by performing linear regression analysis. The correlation coefficients were compared to establish which equation gave the best fit to the experimental data.

D) Electrical Conductivity

For the electrical measurements, the samples were prepared using the same coprecipitation technique using higher purity starting materials (Table 6).

Table 6. Impurities in the high purity materials.

Impurity	Y_2O_3 (ppm)	Impurity	$CaCO_3$ (ppm)
Si	3	Sr	7
Fe	< 3	Fe	7
Al	< 1	Mg	1

The electrical conductivity of the yttria-calcia samples was measured using a two probe technique. Prior to any measurement, it was necessary to platinize both sides of the pellets. This was accomplished by applying a platinum ink to the pellet and firing the pellet in air at 800 C to drive off the organic binder. The platinized pellet was then placed in the "conductivity cell" (Figure 11). Two electrodes, consisting of platinum lead wires welded to platinum foil were placed on either side of the pellet. The pellet was thus sandwiched between the two foils which serve as the electrodes: the lead wires ran down the length of the alumina tube which served as a holder for the conductivity cell. The cell was held in the holder by the force of a spring on the cool end of an alumina push rod. The spring was located in the water cooled brass head attached to the end of the furnace tube. The brass head contained five ports through which the two

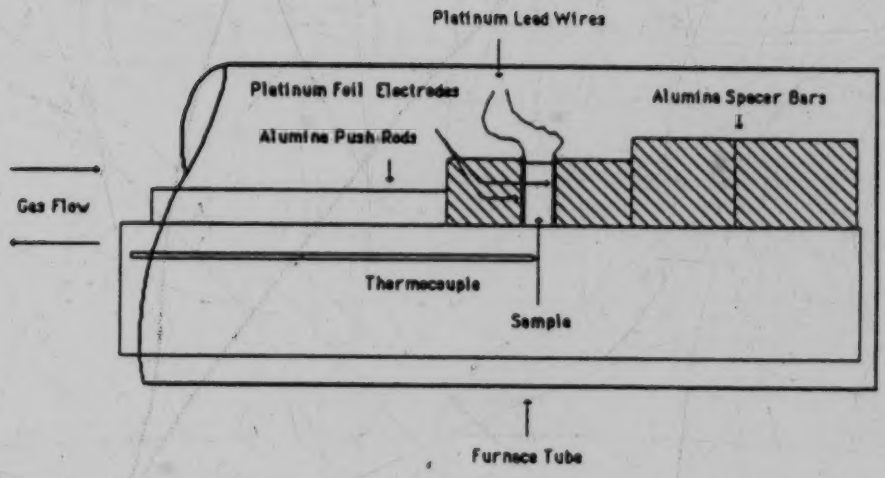

Figure 11. The conductivity cell.

lead wires and a Pt/Pt-13%Rh thermocouple could pass. The remaining two openings served as the gas inlet and outlet ports.

The cell in its holder was placed inside a closed end alumina furnace tube in a Harrop resistance furnace. The tube was sealed by means of an O-ring assembly within the brass head. The cell was placed in the furnace's hot zone where a grounded platinum foil "shield" encased the furnace tube to isolate the cell from stray electrical interference.

The tube furnace temperature was controlled (plus or minus 1 C) by means of a solid-state PID controller and was monitored with the platinum/rhodium thermocouple.

The desired oxygen partial pressure was achieved using pre-analyzed gas mixtures, either $Ar-O_2$ or $CO-CO_2$. The appropriate gas mixtures were dried with a combination of $Mg(ClO_4)_2$, molecular sieves (5A) and "Indicating Drierite", which was used to monitor the drying efficiency. Flow rates were controlled using a calibrated flow meter.

Prior to each run the cell was held at 1000 C for 12 hr. This allowed the two platinum foil electrodes to form a satisfactory contact with the platinized surface of the pellet. The force of the push rod limited the effects of contact resistance at this interface.

The sample cell chamber was purged with the desired gas mixture at a rate of 150 standard cubic centimeters per minute (sccm) for 30 minutes. The gas flow was then lowered

to 50 sccm to allow the cell to achieve thermal equilibrium.

The conductivity of the cell was measured indirectly with a digibridge by recording the variation of the resistance with the changing temperature and oxygen pressure at a frequency of 1000 Hz. The resistance was then related to the conductivity by equation (99):

$$\sigma = L/RA \qquad \text{(Eq. 99)}$$

where R is the measured resistance. L is the thickness of the pellet, and A is the cross-sectional area of the pellet.

V. RESULTS AND DISCUSSION

A) Phase Study

When CaO is dissolved in Y_2O_3, the decrease in the overall charge resulting from the introduction of lower valent cations can be compensated by the formation of either cation interstitials or oxygen vacancies. The theoretical density of the compound is expected to decrease more rapidly in the latter case than in the former. Experimental data presented in Figure 12 shows that the density of the Y_2O_3-CaO pellets, although less than the theoretical amount, does decrease. The slope is similar to that predicted by the anion vacancy model, where the density of Y_2O_3 with x atomic % CaO is given by the mass of $Y_{2-x}Ca_xO_{3-x}$ divided by the theoretical volume (based on the measured lattice parameter)[**].

The experimental density of the pure Y_2O_3 pelletsis lower than those obtained in the mixed compounds, suggesting that CaO may act as a sintering aid in addition to its role in creating oxygen vacancies. In comparing the experimental data to the anion vacancy model, this point was ignored.

The demonstration of the existence of oxygen vacancies indicates that the following defect reaction is primarily responsible for defect formation:

$$CaO = Ca'_Y + 1/2\ V^{\cdot}_O + O^{x}_O \qquad \text{(Eq. 100)}$$

and that the vacancy concentration will be:

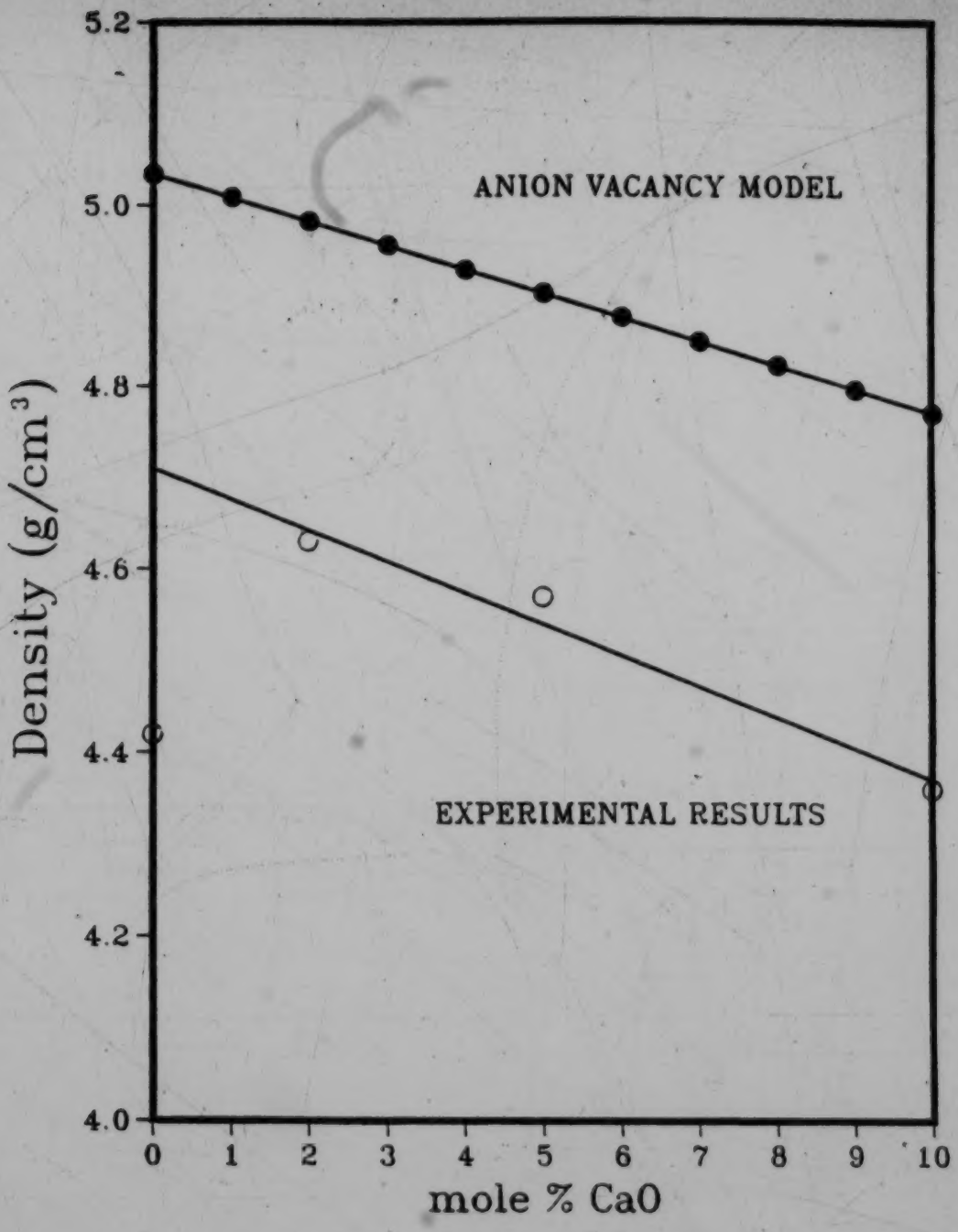

Figure 12. A comparison of experimental densities with those predicted by the anion vacancy model.

$$[V'_o] = 1/2\,[Ca'_v] \qquad \text{(Eq. 101)}$$

Figure 12 also suggests that 10 % CaO can exist in solid solution with Y_2O_3; this was confirmed by the phase study.

The lattice parameter values were calculated by plotting each lattice parameter (as defined by a specific peak) against a function of the peak diffraction angle and extrapolating the curve back to $2\theta = 180°$. The lattice parameter at a peak was given by:

$$a = \frac{\lambda (h^2 + k^2 + l^2)}{2 \sin \theta} \qquad \text{(Eq. 102)}$$

and the function of θ used was $\cos^2 \theta / \sin \theta$.

To improve the accuracy of the technique only those peaks whose 2θ angles were greater than 60° were used in the regression and their locations were measured to plus or minus 0.01°. This meant using the peaks of those planes with $(h^2+k^2+l^2)$ greater than $(4^2+4^2+4^2)$, the (444) peak occurs at approximately 60° (2θ). Table 7 shows the "d" spacings and peak intensities for the most intense reflections in Y_2O_3 and CaO[81]. Appendix 1 shows the complete ASTM card file for the x ray powder diffraction patterns of Y_2O_3 and CaO.

CaO peaks were evident in the original precipitated powder but could not be seen in the sintered compact, indicating some degree of solid solution in the sintered body. From Figure 13, the lattice parameter of pure yttia

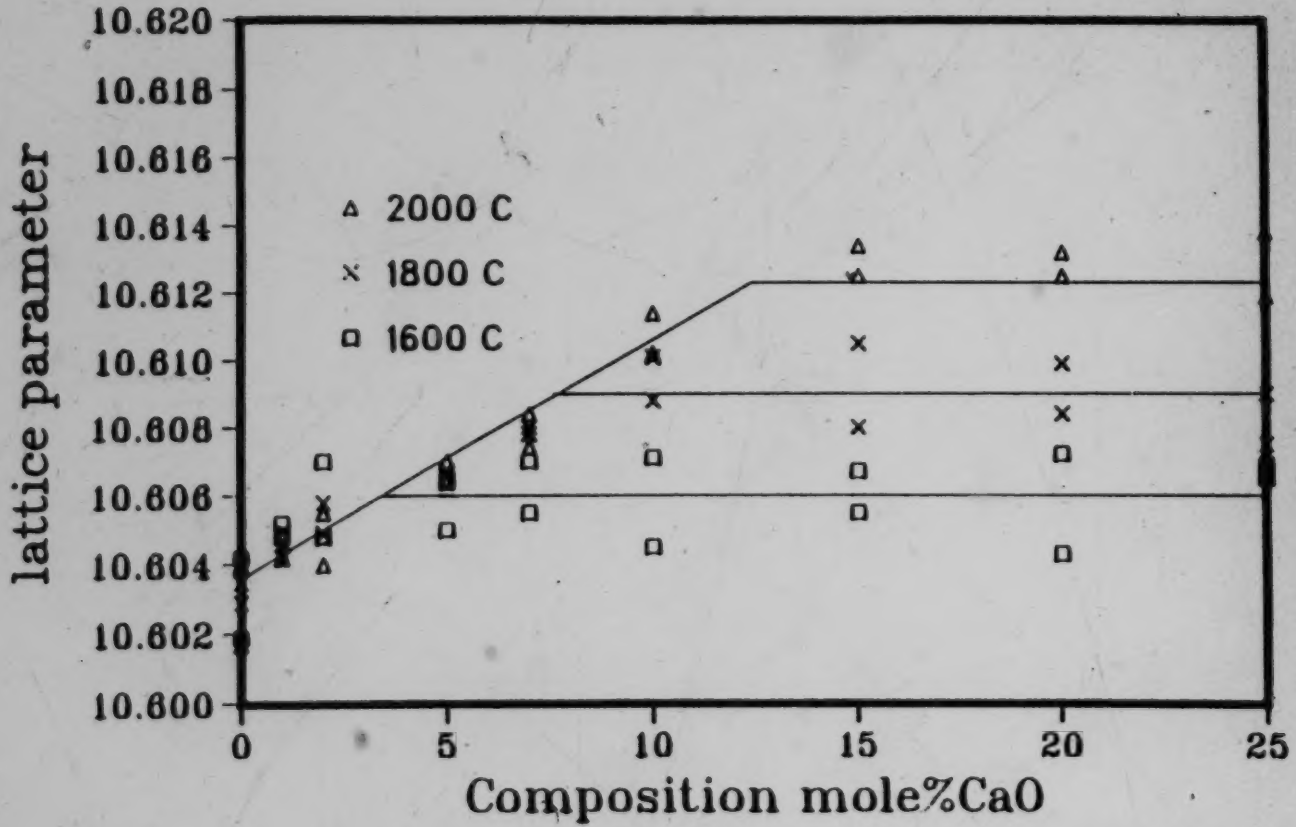

Figure 13. The variation in the lattice parameter of Y_2O_3 in the solid solution temperature range.

was determined to be 10.6035 A. As the amount of CaO dissolved in Y_2O_3 increased, the lattice parameter of the C-type structure increased up to a maximum of 10.6123 A at 2000 C. This corresponds to approximately 12.4 % dissolved CaO.

Table 7. The "d" spacings for the 10 most intense reflections of Y_2O_3 and CaO[81].

Y_2O_3			CaO		
hkl	d(A)	I/Io	hkl	d(A)	I/Io
222	3.060	100	200	2.405	100
440	1.874	46	220	1.701	45
622	1.599	31	111	2.778	34
400	2.652	30	311	1.451	10
211	4.340	16	420	1.076	9
510	2.080	12	422	0.982	9
332	2.261	8	600	0.802	6
662	1.216	8	222	1.390	5
411	2.500	7	400	1.203	4
631	1.563	7	331	1.104	4

At temperatures below 1400 C, no change in the lattice parameter was observed; there appeared to be no solid solubility between the two components. Above 1400 C the lattice parameter increased as the amount of CaO increased until it reached the solubility limit at each temperature. The solubility limits corresponding to the various temperatures are shown in Table 8 and a revised phase diagram is shown in Figure 14.

No evidence for either CaY_4O_7 or CaY_2O_4 was found. Perhaps the temperature was not high enough to favour formation (although another study[10] observed these compounds

above 1850 C) or the amount of either compound was insufficient to be detected (less than 5%). Similarly, no evidence of the hexagonal crystal structure of Y_2O_3 was observed, indicating that the polymorphic transformation occurs at temperatures above 2000 C.

Table 8. A summary of the solubility limits of CaO in Y_2O_3.

Temperature °C	Solubility Limit mole %CaO
1200	0
1400	0
1600	3.4
1800	7.4
2000	12.4

This evidence suggests that the complex polymorphic transformations that are common in other rare earth-alkaline earth oxide phase diagrams only occur above 2000 C in the yttria rich region of the Y_2O_3-CaO system and perhaps only the cubic (C) to hexagonal transformation takes place[82].

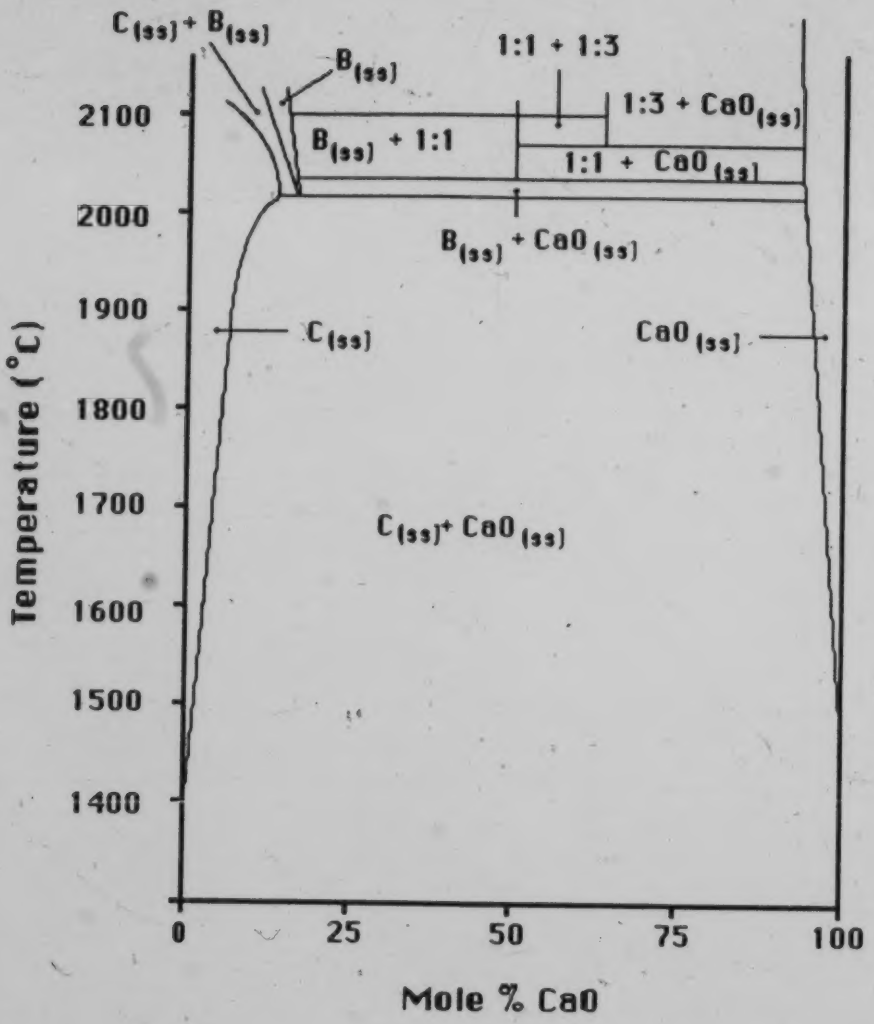

Figure 14. Modified Y_2O_3-CaO phase diagram.
(above 2100 C the diagram stays the same as figure 4)

B) Kinetics of Exsolution

The decomposition curves for all the measured temperatures are presented in Figures 15 and 16. These curves are all sigmoidal, and suggest that the exsolution of CaO from Y_2O_3 occurred by consecutive nucleation and growth processes.

To explore this conclusion, the experimental data from the exsolution kinetics was compared to the models seen earlier in Table 2. An arbitrary time was chosen, and the fraction reacted, α , corresponding to that time, was substituted into the $f(\alpha)$ for each of the ten models and each $f(\alpha)$ was plotted against time. The correlation between $f(\alpha)$ and time was evaluated using a linear least-squares regression program. The model that yielded the highest correlation coefficient was deemed to be the most applicable. Figures 17-19 show the comparison of these models for the kinetics of exsolution at 1500 C. Clearly the three-dimensional nucleation and growth model (A3) provided the best fit to a straight line at this temperature.

The correlation coefficients for all the models as well as their final rankings are shown in Table 9. The three-dimensional nucleation and growth model is the most appropriate across the temperature range studied here.

Unfortunately, this model failed to provide any information about the growth mechanism; the more elaborate model of Hulbert was used to further analyze the system.

In Hulbert's model (Eq.98) a plot of $\ln[\ln(1/(1-\alpha))]$

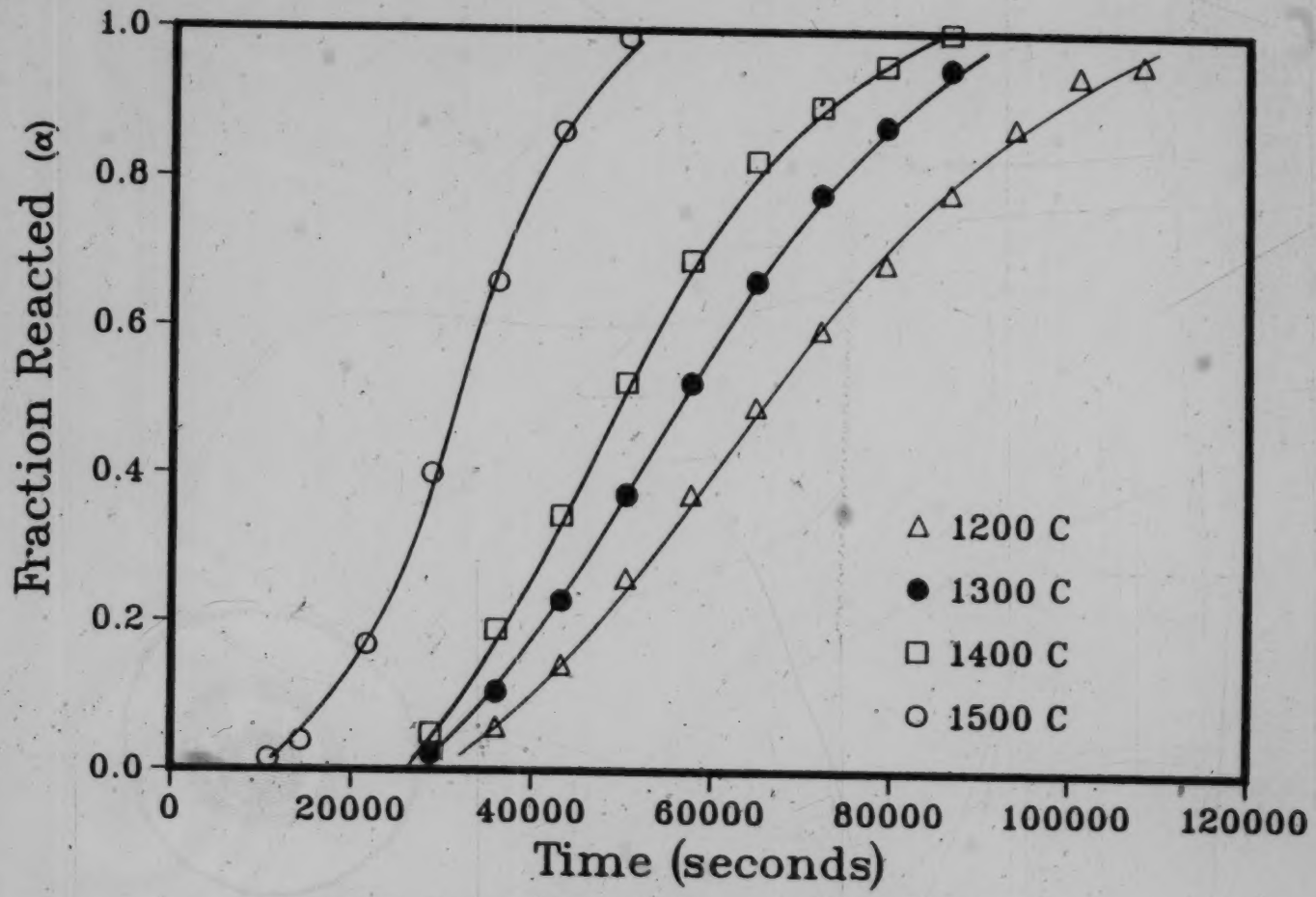

Figure 15. Decomposition curves for Y_2O_3–10%CaO at 1200 C to 1500 C

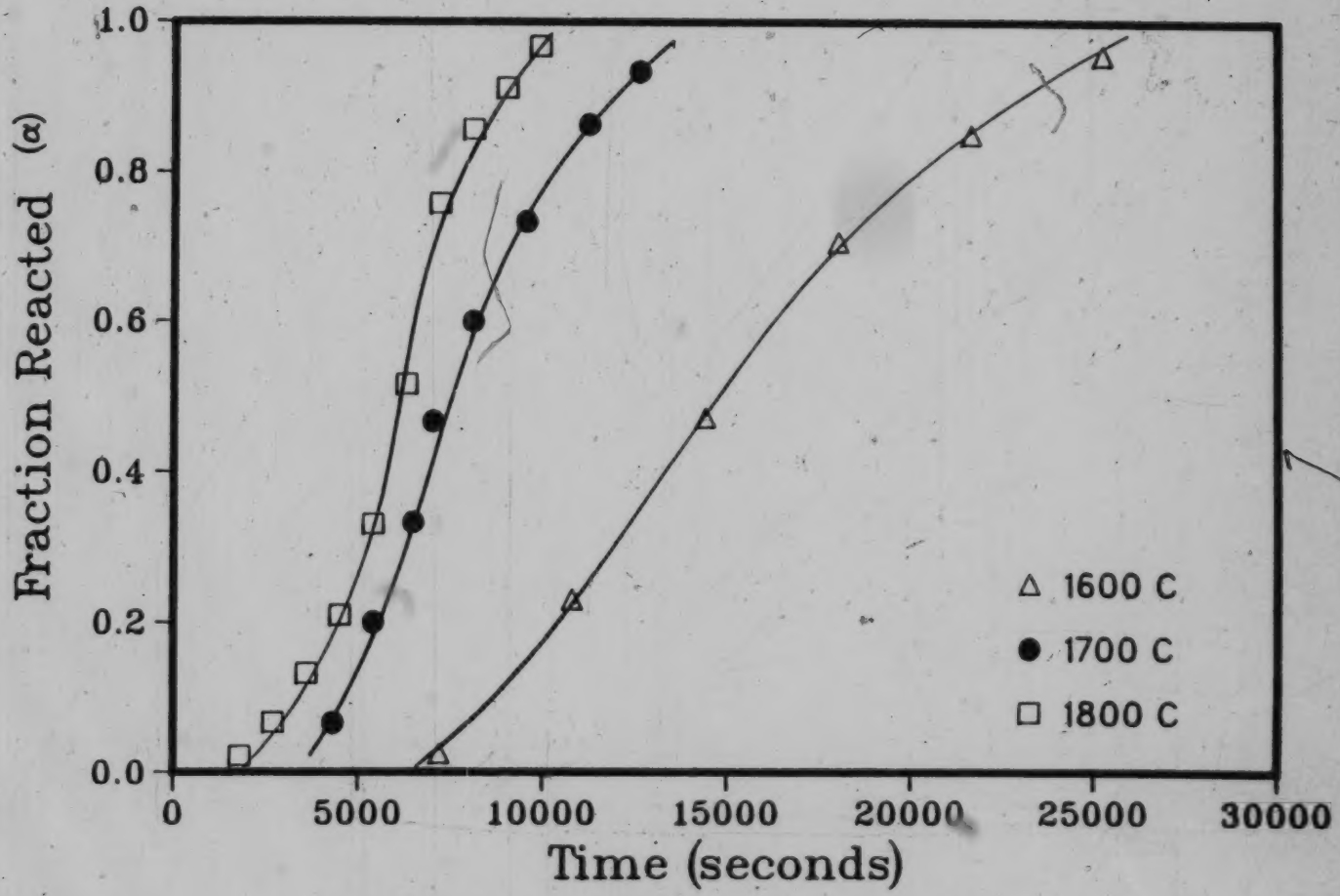

Figure 16. Decomposition curves for Y_2O at 1600 C – 1800 C

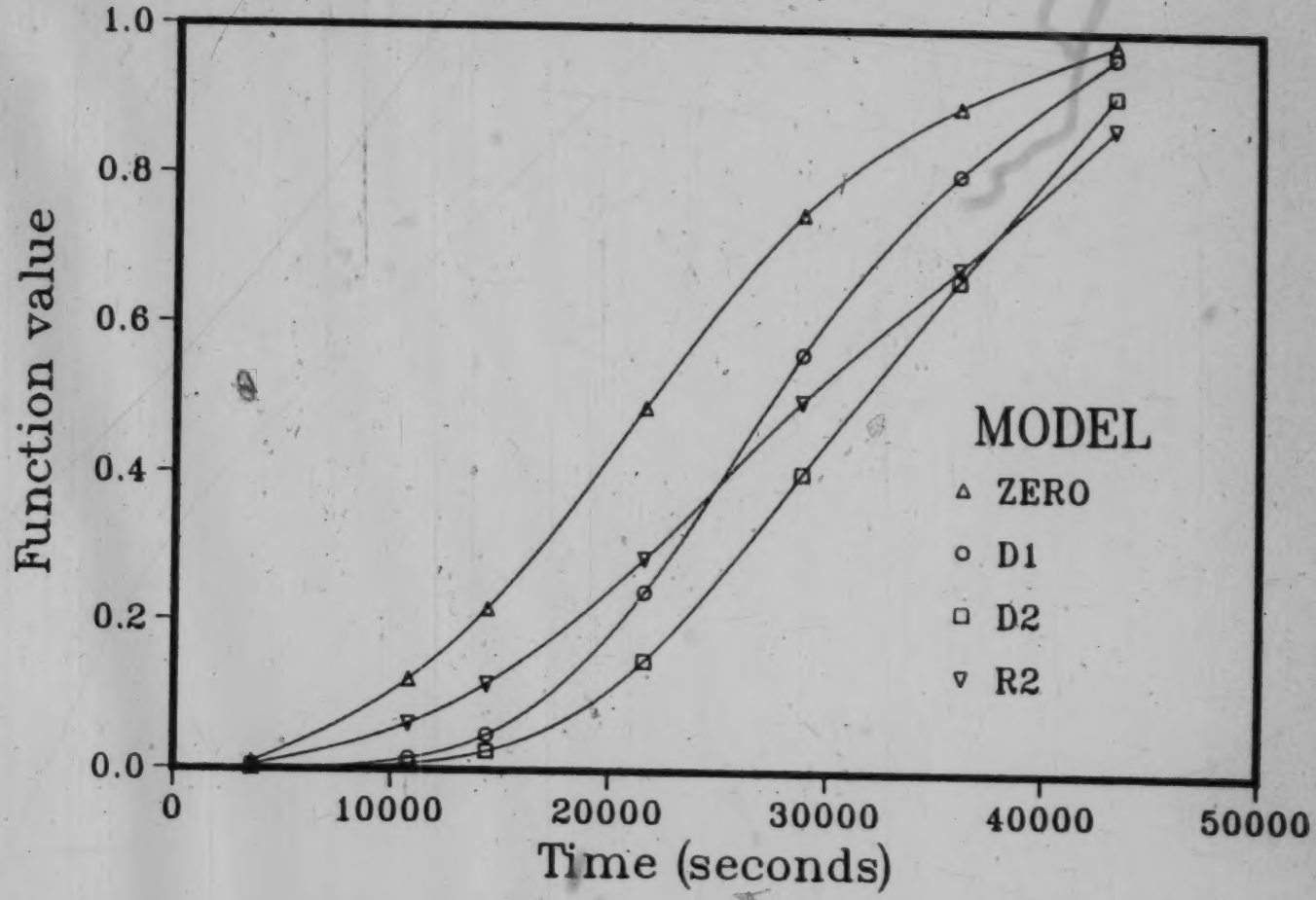

Figure 17. A comparison of the solid-state models zero, D1, D2, and R2 at 1500 C.

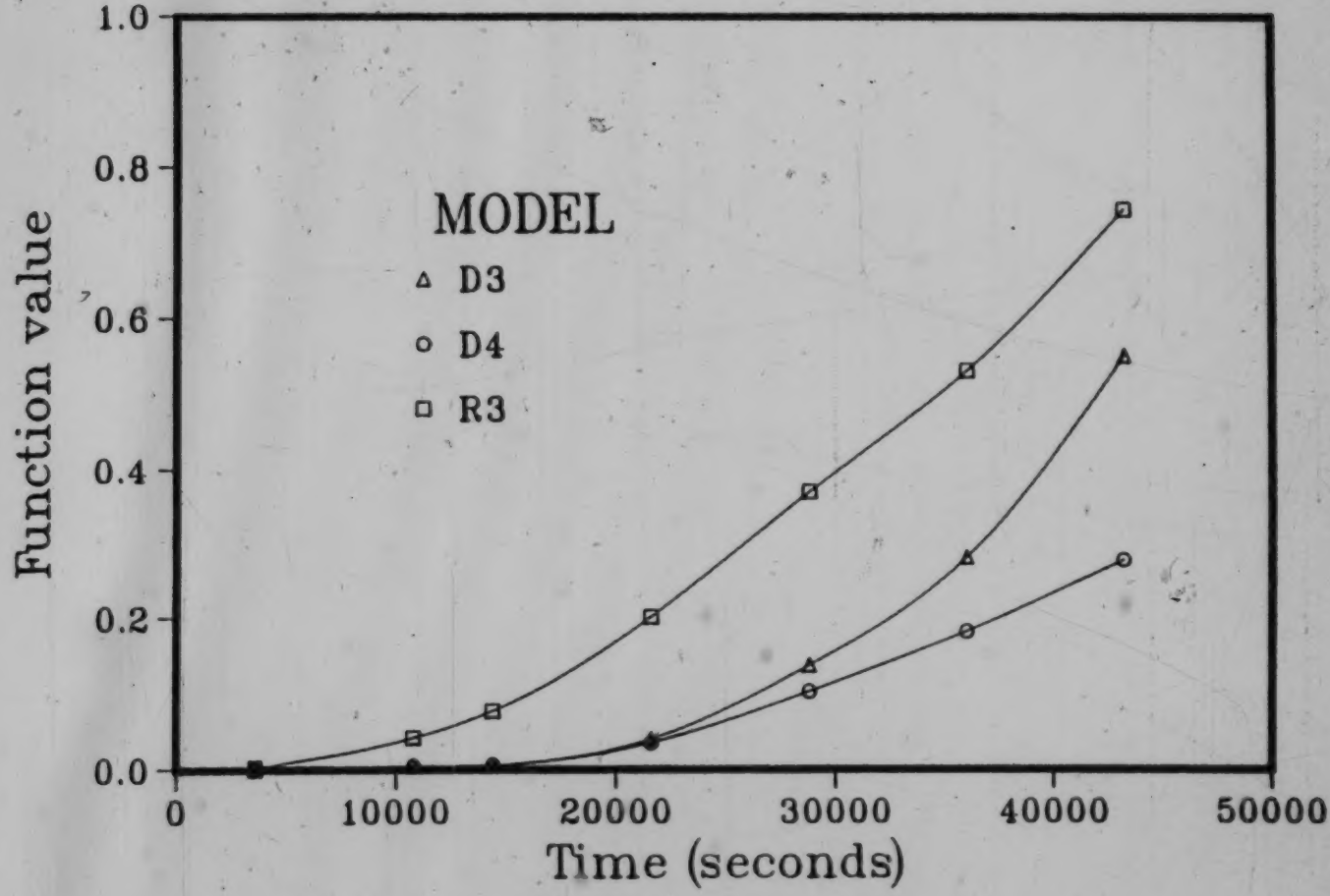

Figure 18. A comparison of the solid-state models D3, D4, and R3 at 1500 C.

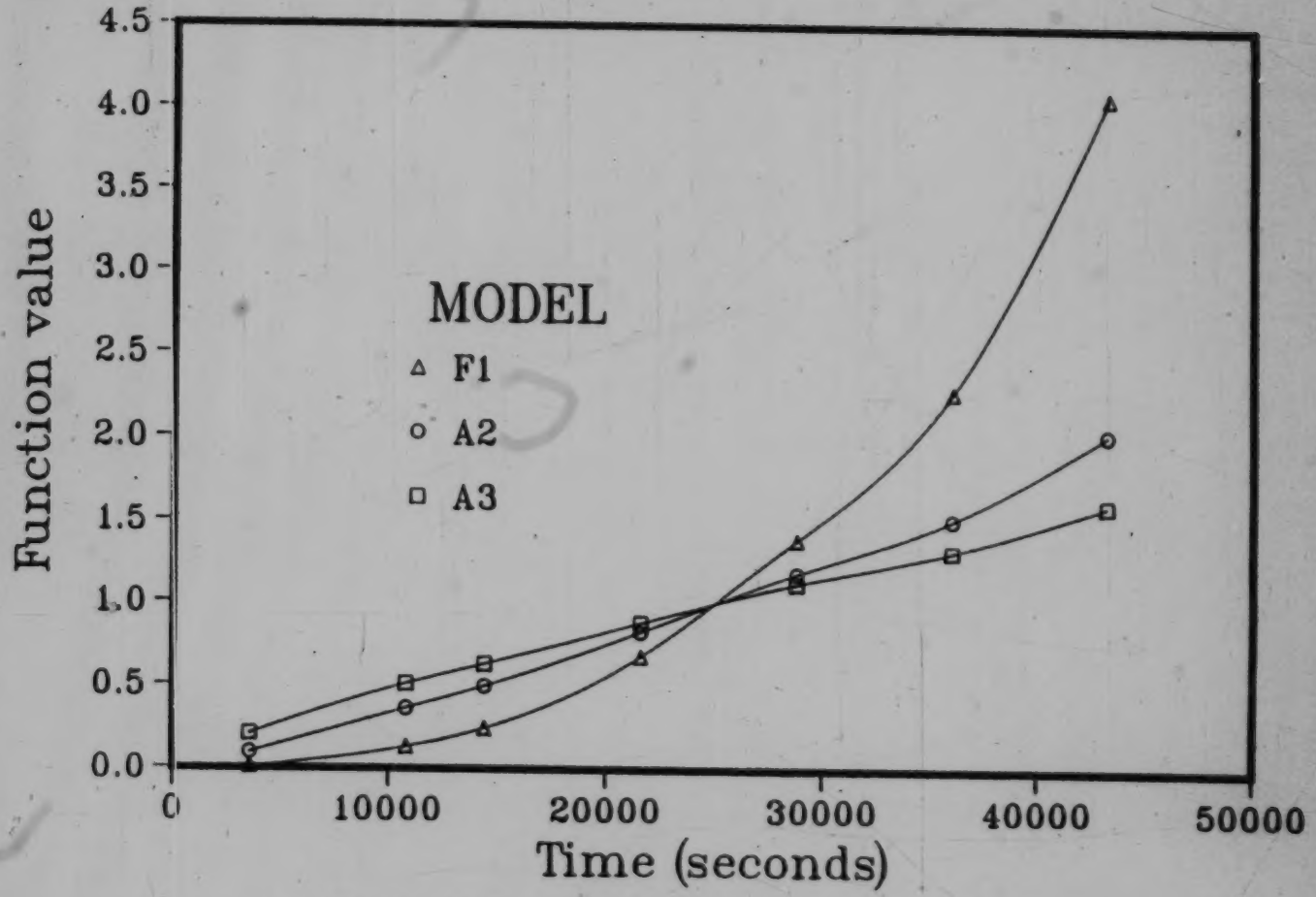

Figure 19. A comparison of the solid-state models F1, A2 and A3 at 1500 C.

against ln (time) should yield a straight line with an intercept ln k, and a slope m, where "m" gives an indication of the growth characteristics. Figures 20 and 21 show these plots for the experimental data (where α was between 0.2 and 0.9)[48] and Table 10 summarises the value of "m" for the various temperatures studied. Clearly, there is a change between 1500 C and 1600 C.

Table 9. A comparison of the correlation coefficients of the various models.

Temp. °C	Z	D1	D2	D3	D4	F1	R2	R3	A2	A3
1200	.993	.987	.965	.910	.949	.953	.994	.985	.994	.997
1300	.997	.976	.952	.896	.936	.951	.992	.984	.997	.998
1400	.981	.989	.981	.883	.963	.866	.996	.980	.997	.998
1500	.993	.956	.925	.837	.899	.827	.974	.954	.977	.995
1600	.988	.973	.958	.900	.943	.937	.987	.980	.995	.999
1700	.984	.993	.983	.953	.976	.943	.998	.976	.990	.996
1800	.973	.983	.985	.957	.982	.986	.992	.994	.996	.993
Final Ranking	4	5	7	10	8	9	3	6	2	1

Table 10. Summary of the "m" value for the experimental temperature range.

Temperature °C	"m"
1200	3.14
1300	3.38
1400	3.34
1500	3.42
1600	2.88
1700	2.97
1800	2.97

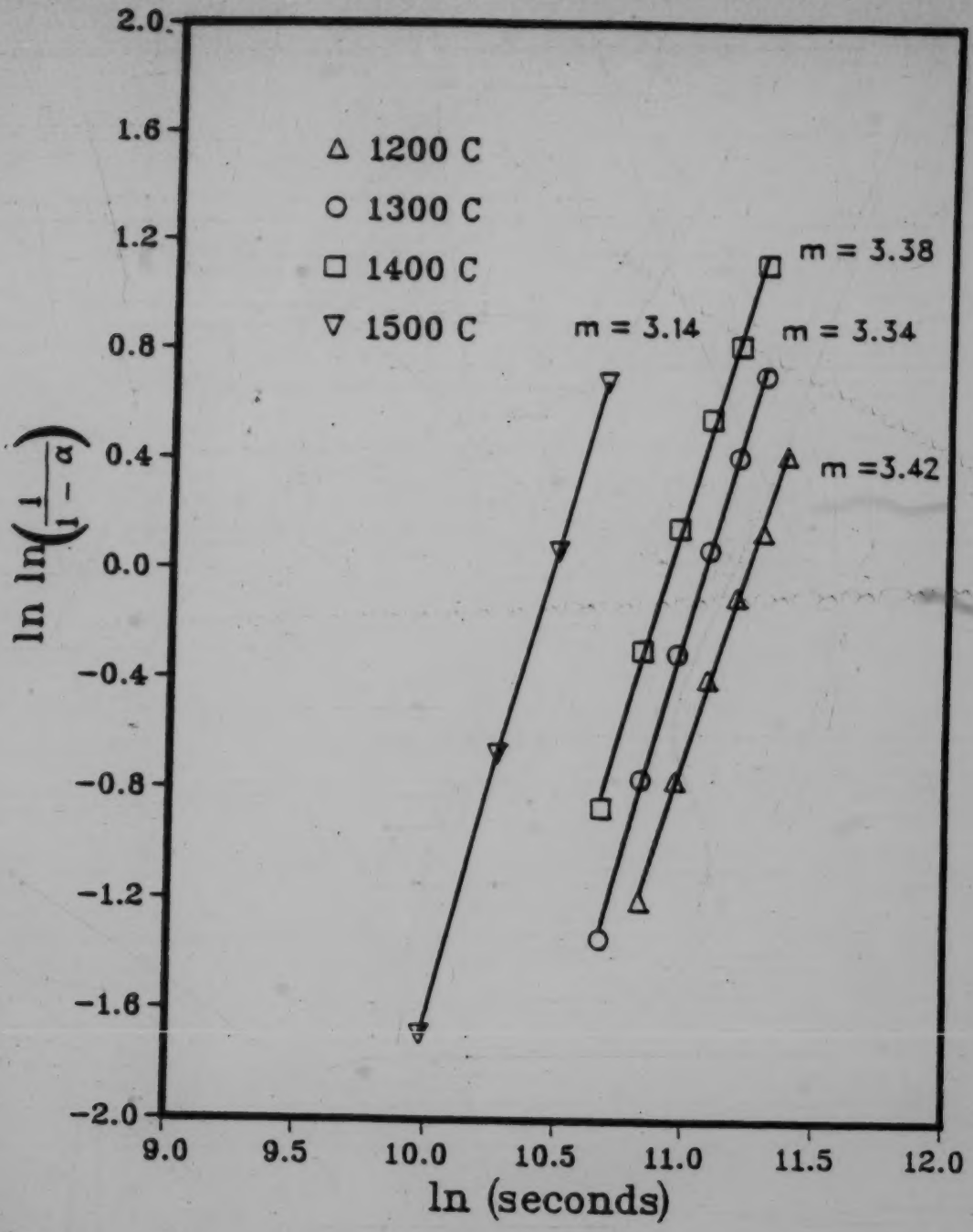

Figure 20. Determination of "m" from 1200 C to 1500 C.

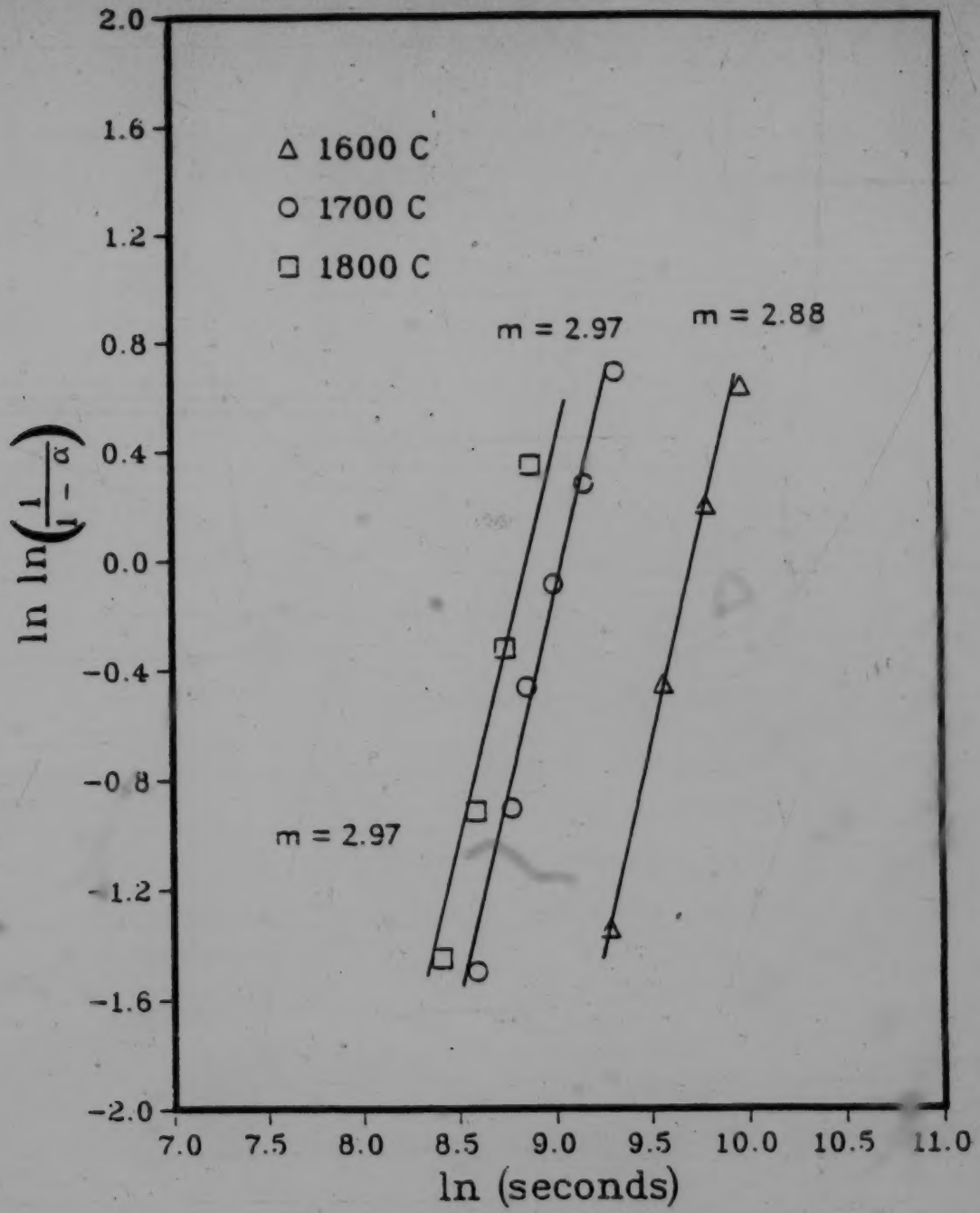

Figure 21. Determination of "m" from 1600 C to 1800 C.

In the initial region (1200-1500 C), "m" had an average value of 3.33 indicating the growth mechanism was phase boundary controlled (Table 4), the nucleation rate was decreasing and the precipitate was spherical. In the 1600-1800 C range the average value of "m" was 2.94 which was interpreted as indicating that either the nucleation rate had dropped to zero (i.e., saturation of point sites) or the growth had become two-dimensional (i.e., changed from spherical to disk morphology).

The Hulbert model was used to describe the growth in the two regions:

Range 1 (1200 C - 1500 C):

$$\ln \frac{1}{1-\alpha} = kt^{3.33} \qquad \text{(Eq. 103)}$$

Range 2 (1600 C - 1800 C):

$$\ln \frac{1}{1-\alpha} = kt^{2.94} \qquad \text{(Eq. 104)}$$

In order to determine k, the experimental data was substituted into either equation (103) or (104). Using these values of k and the inverse of the absolute temperature an Arrhenius plot was developed (Figure 22). The Arrhenius plot indicated that the transition between range 1 and 2 oceured at a lower temperature (approximately 1420 C) than indicated by the Hulbert model.

The slope of each curve on the Arrhenius plot is equal to the activation energy (E.) divided by the ideal gas

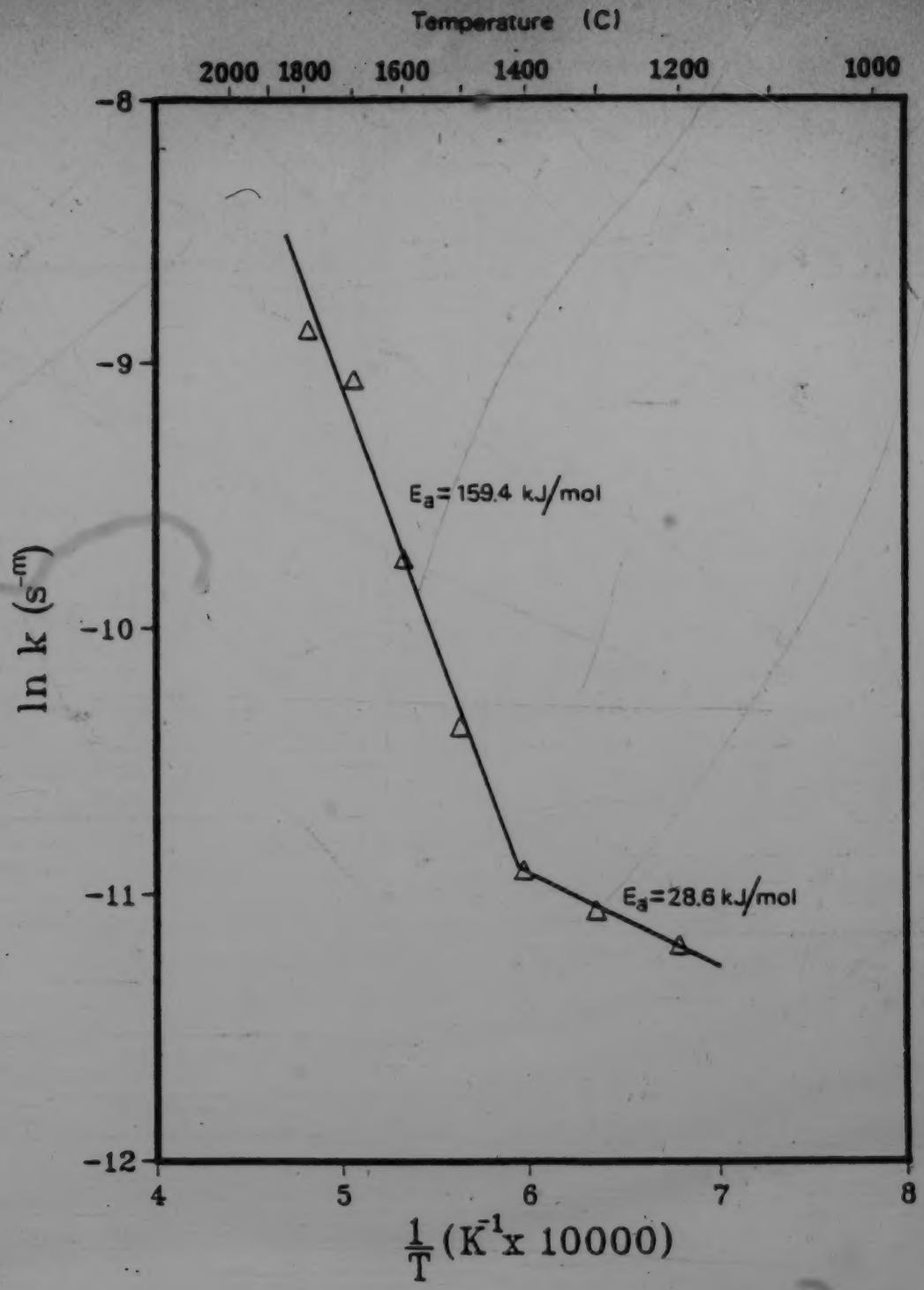

Figure 22. Arrhenius plot for the Y_2O_3-CaO system.

constant (R). The activation energy for region 1 was 28.6 kJ/mol; for region 2, it was 159.4 kJ/mol. For the second region, the value of E. is similar to that given for the NiO-CaO system (196 kJ/mol)[42]. The activation energy for the second region was between the value determined by Ando[9] for oxygen ion diffusion (191 kJ/mol) and that found by Norby and Kofstad for hydrogen ion diffusion in yttria (150 kJ/mol)[43]. The activation energy for the native proton is twice that of hydrogen (301 kJ/mol)[10]. The lower activation energy in stage 1 suggested some sort of short circuit diffusion: perhaps grain boundary or surface diffusion dominated at lower temperatures.

C) Electrical Conductivity

The results of the electrical conductivity measurements for three compositions (0%, 5%, and 10% CaO) were plotted in Figures 23, 24, and 25 for four different temperatures. A fifth temperature (600 C) was also used, but the results proved inconsistent and irreproducible.

In the case of pure yttria, both a positive and a negative dependence of the conductivity on the partial oxygen pressure were seen, as shown in Figure 23 for 1200 C. At high oxygen partial pressures, a positive dependence (indicating "p" type conductivty) was seen, while at low partial pressures a negative dependence indicated "n" type conductivity. At 1400 C there was no evidence of any "n" type conductivity simply because the gas mixtures would not produce a low enough partial oxygen pressure to produce the

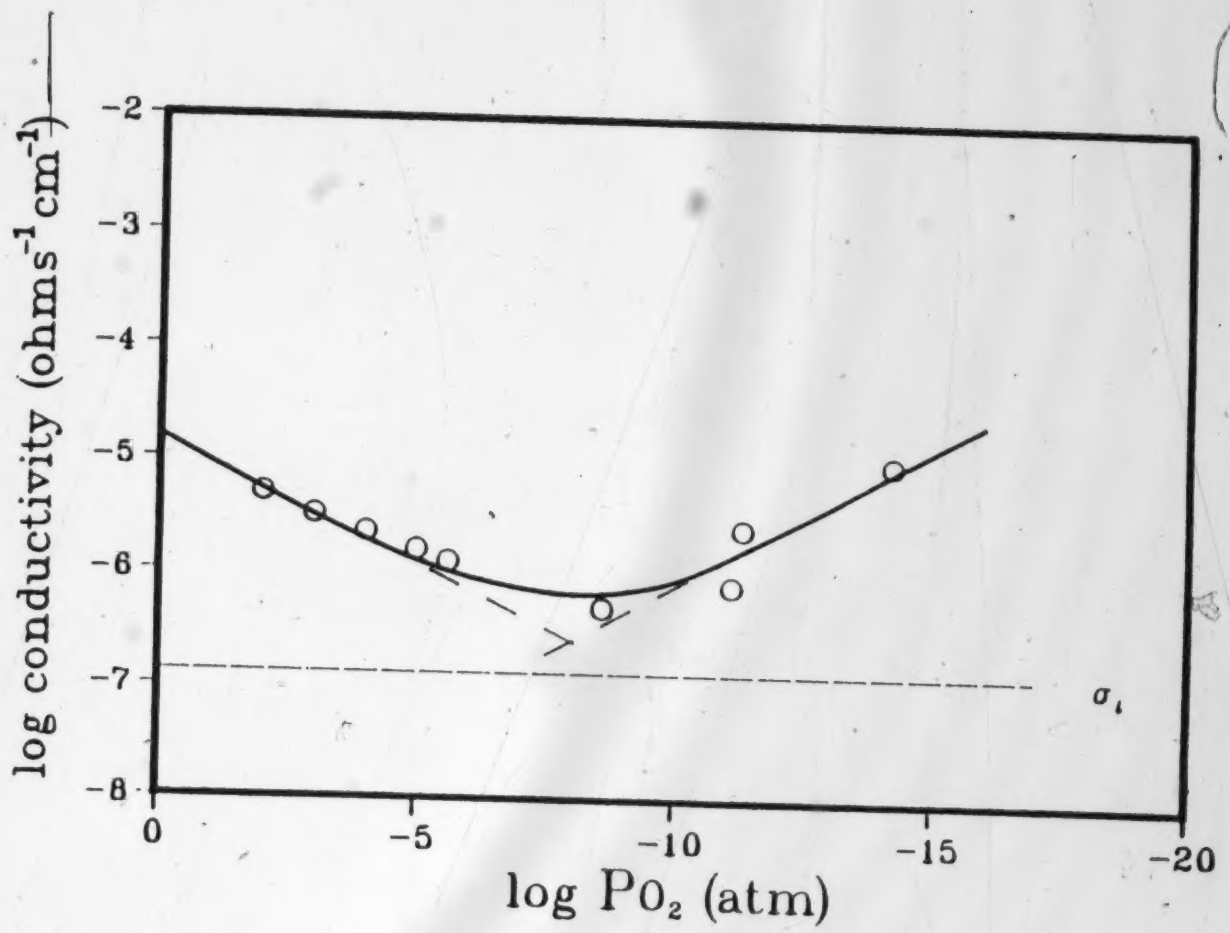

Figure 23. The dependence of the conductivity of yttria on the P_{O_2} at 1200 C.

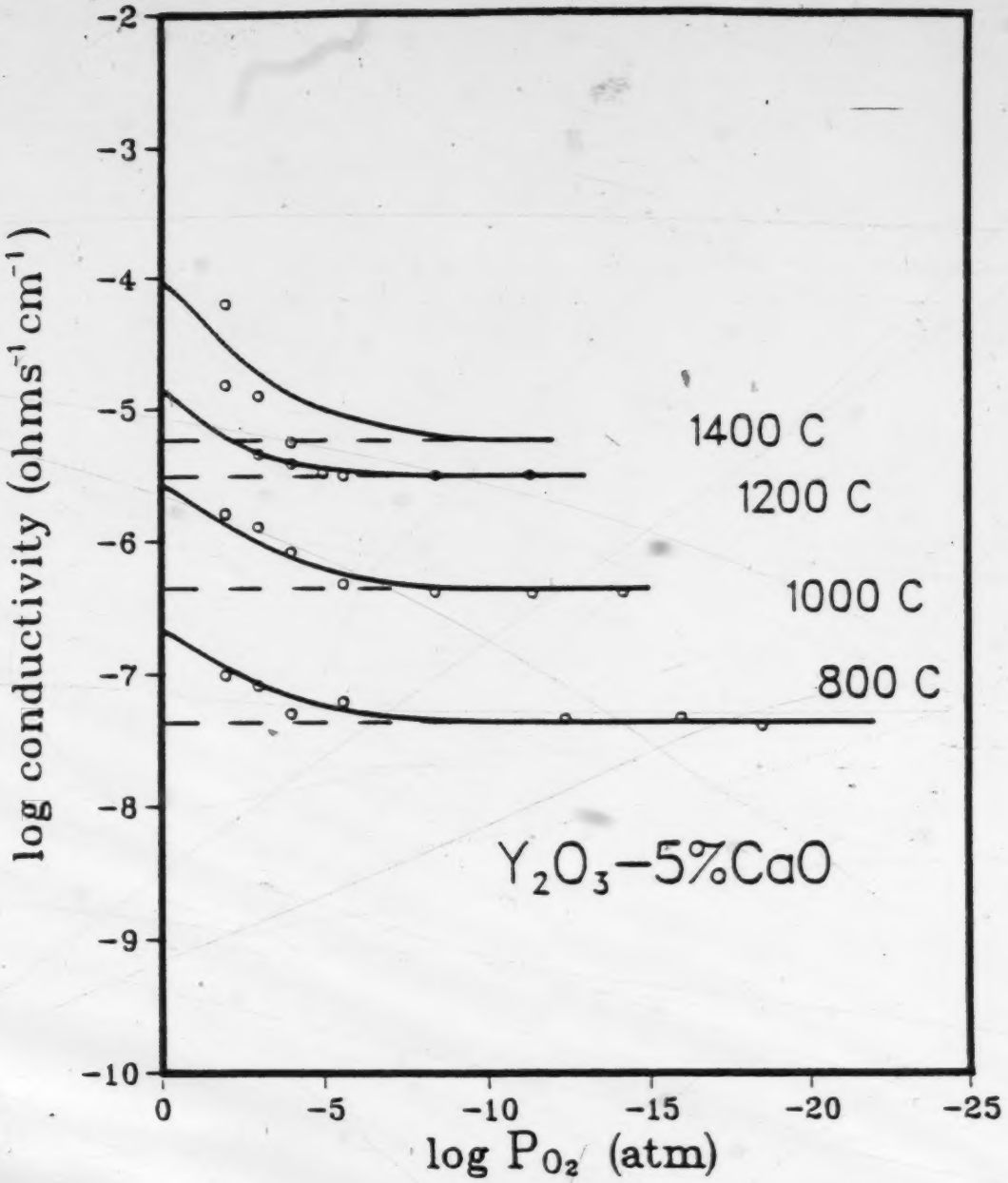

Figure 24. Conductivity isotherms for Y_2O_3-5%CaO.

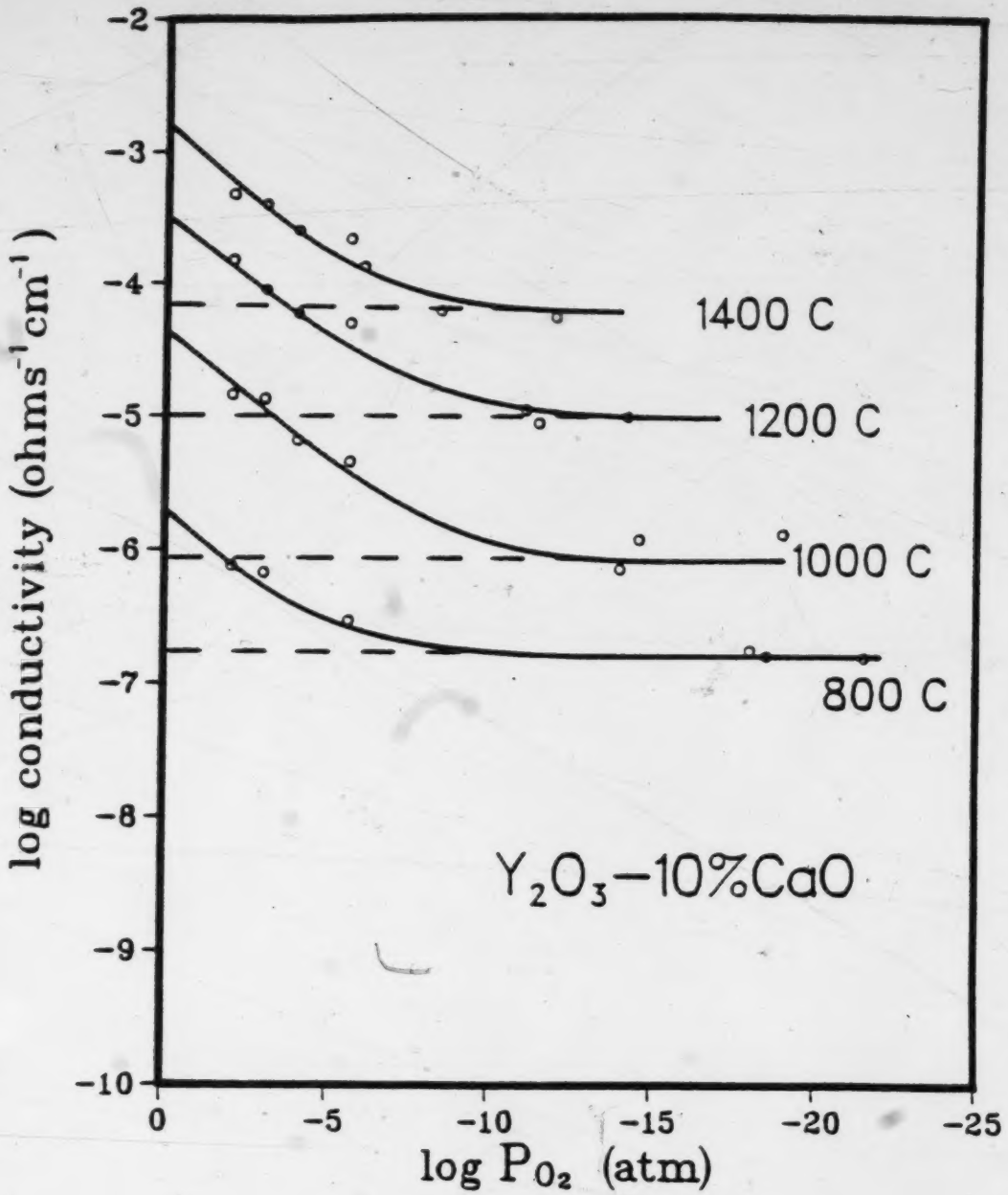

Figure 25. Conductivity isotherms for Y_2O_3-10%CaO.

"n" type conductivity.

The "p" or "n" type conductivity were separated from the total conductivity as follows. At the low and high partial pressures the total conductivity curve was approximately linear. A tangent to the conductivity isotherm drawn at each of these points and extrapolated to the center intersected at the point were "p" = "n". This point was located under the minimum of the total conductivity curve. Subtracting the value of "p" plus "n" from the total conductivity at that point yielded the ionic contributuion. The ionic conductivity was assumed to be constant so the "p" or "n" contribution at any partial oxygen pressure could be determined. Subtracting the ionic conductivity from the total gave the "p" or "n" contribution, the log of which was plotted against the log of the partial oxygen pressure (Figure 26). The slope of the resulting straight line indicates the pressure dependence of the p type conductivity.

In the 0% case, the "p" type conduction was proportional to $p \propto Po_2^{1/4.3}$, while the "n" type was proportional to $n \propto Po_2^{-1/4.3}$. These were close to the theoretical values for a mixed ionic-electronic conductor, where the pressure dependence was given by

$$n = \frac{K_1}{p} \propto Po_2^{-1/4} \qquad \text{(Eq. 105)}$$

regardless of the type of defect. This is true for the extrinsic region where the concentration of the defects is

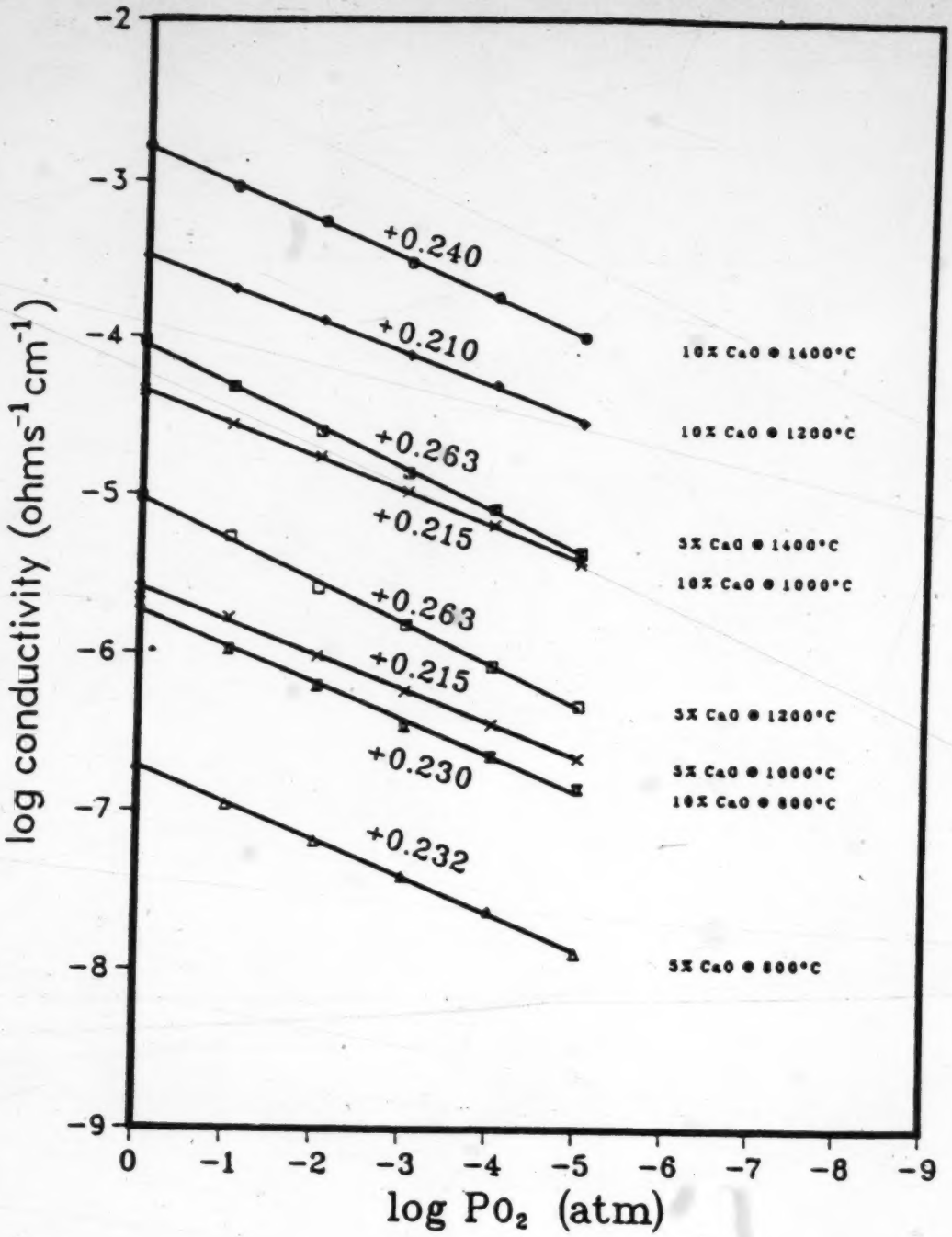

Figure 26. The dependence of the "p" type conductivity on the partial oxygen pressure.

controlled by the amount of impurities.

In the 5% and 10% cases (Figures 24 and 25), the notable differences are the lack of any "n" type conductivity in the pressure range studied and the presence of a region of constant conductivity, indicating virtually pure ionic conduction.

As before, the "p" type conduction was separated from the total by subtracting the ionic contribution (the value at which the total conductivity was constant). The resulting pressure dependences of the "p" type conductivity for 5% and 10% CaO are also shown in Figure 26.

In these two cases the predominant defects were oxygen vacancies and the defect concentration was controlled by the dopant concentration, so equations (37) and (38) were important:

$$O^x_o = V^{\cdot\cdot}_o + 2e' + 1/2\ O_2 \qquad \text{(Eq. 37)}$$

$$K_v = [V^{\cdot\cdot}_o]n^2 P_{O_2}^{1/2} \qquad \text{(Eq. 38)}$$

Rearranging (Eq. 38) gives:

$$n = (K_v/[V^{\cdot\cdot}_o])^{1/2} P_{O_2}^{-1/4} \qquad \text{(Eq. 106)}$$

and since

$$[V^{\cdot\cdot}_o] = 1/2\ [CaO] \qquad \text{(Eq. 101)}$$

and because the [CaO] is approximately constant, then

$$n \propto P_{O_2}^{-1/4} \qquad \text{(Eq. 107)}$$

In the 5% case, the "p" type conductivity was proportional to $Po_2^{1/4.4}$; the 10% samples showed a pressure dependence of 1/4.8.

The pressure dependence is less than that predicted by theory. Norby and Kofstad[84] suggest this is due the the presence of electronic defects.

The total conductivity of Y_2O_3 and Y_2O_3-CaO electrolytes was plotted against the inverse of the absolute temperature in an Arrhenius plot (Figure 27). The curves at a partial oxygen pressure of 0.1 atm represent mainly p type conduction, while those at lower partial oxygen pressures represent almost pure ionic conduction.

The apparent activation energies found in this study compared favourably with those of other researchers. For pure yttria, previous values have varied between 138 kJ/mol[29] and 187 kJ/mol[28] (at approximately 10^{-8} atmospheres and 0.21 atmospheres of oxygen respectively). The only reported data for a mixed Y_2O_3-CaO compound comes from Etsell who found an activation energy of 152 kJ/mol for a 5% CaO pellet (at a partial pressure of oxygen of 0.06 atmospheres).

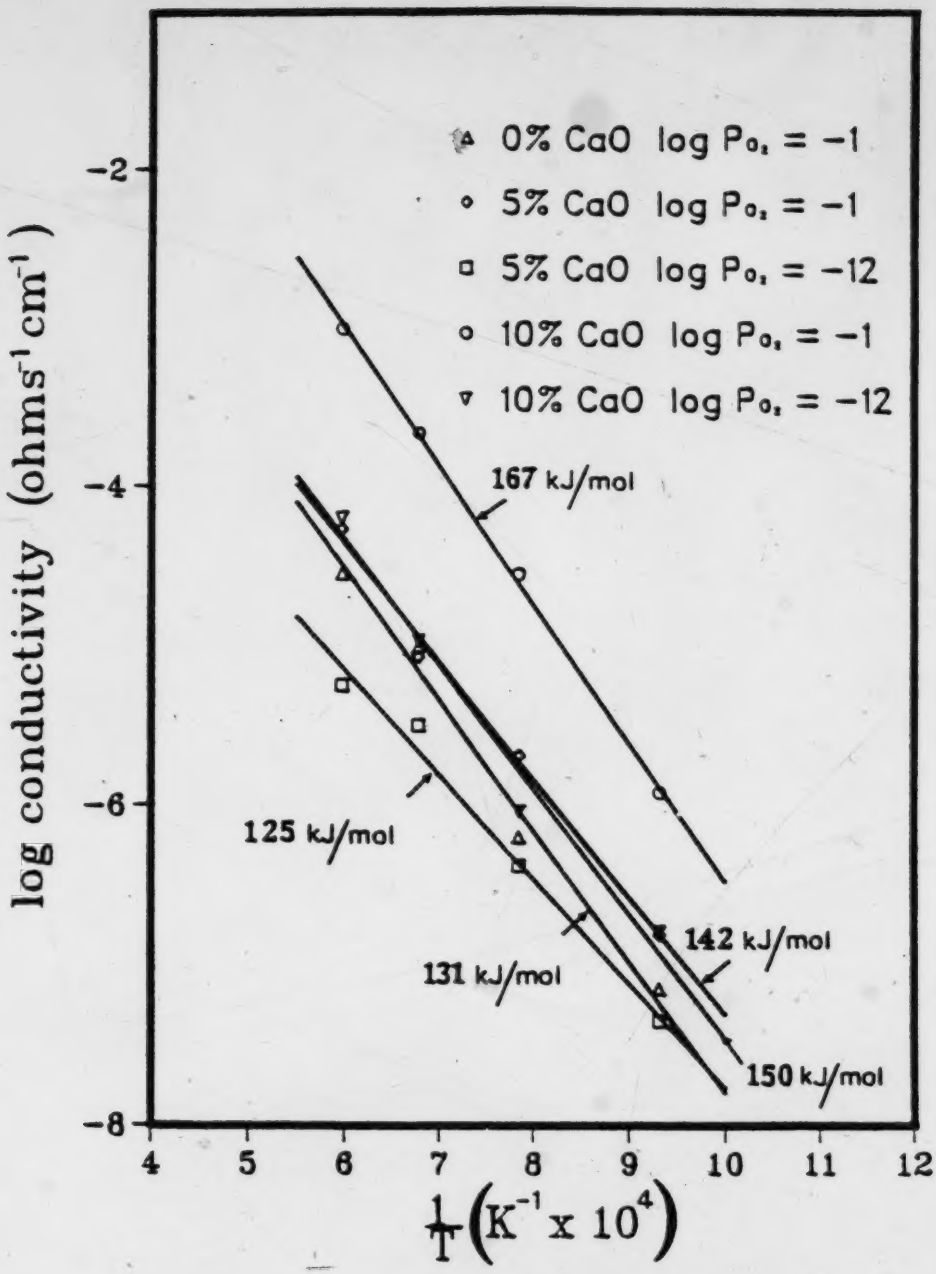

Figure 27. Arrhenius plots for total conductivity.

VI. CONCLUSIONS

This study was undertaken to evaluate the possibility of using calcia stabilized yttria as a ceramic electrolyte. The investigation involved three stages: first a phase study to determine the extent of the solid solubility, second, a kinetic study to examine the exsolution rate of the ceramic, and third, a conductivity study to evaluate the electrical properties of the material.

The results of the phase study indicated that a region of solid solubility did exist between CaO and Y_2O_3 from 1400 C to 2000 C. The presence of the dissolved CaO was shown to produce oxygen vacancies in the oxide, which were expected to aid oxygen ion conductivity.

For a material to serve as an electrolyte, the ceramic must remain stable at operating temperatures. For the material to meet this criterion, the CaO that was dissolved in the Y_2O_3 had to remain dissolved long enough for the ceramic to be useful as an electrolyte. The exsolution kinetics indicated that, over a wide range of temperatures, 1200 C to 1800 C, the material remained stable for a sufficiently long time (given that the response time of the material was satisfactory).

An Arrhenius plot showed that the exsolution kinetics involved two regions. In both cases, precipitation occurred by a nucleation and growth process: an analytical approach revealed that the precipitate was spherical. The activation energy in the first region was quite small (28 kJ/mol), as

opposed to the activation energy in the second region (159 kJ/mol). The activation energy of the second region suggested that oxygen ion diffusion was significant.

Electrical measurements showed that Y_2O_3 and Y_2O_3-CaO solutions exhibit some ionic conductivity. Pure yttria showed only a small degree of ionic conductivity, whereas the mixed compound showed significant regions of ionic conductivity below partial oxygen pressures of 10^{-10} atm and down to at least 10^{-18} atm.

These results suggest that Y_2O_3-CaO compounds may serve as a successful electrolyte. It seems that they will act as a purely ionic conductor below around 10^{-10}atm. Further studies need to be done to determine the exact ionic contribution before the definitive picture of the compounds ionic behavior can be characterized.

REFERENCES

1) W. Nernst, Z. Electrochem., 6, (1899) p.41.

2) C. Wagner, Naturwissenschaften., 31, (1943) p. 265.

3) K. Kiukkola and C. Wagner, J. Electrochemical Society, 104, (1957) p. 379.

4) W.D. Kingery et al., J. Am. Ceram. Society. 42 (1959) p. 393.

5) T.A. Wheat, "Developement of a ZrO_2 electrolyte for use in a steel making oxygen probe", Energy Mines and Resources, CANMET report 76-13.

6) G.V. Samsonov, "The Oxide Handbook", IFI/Plenum Press, New York (1973).

7) C.D. Wirkus, M.F. Berard and D.R. Wilder. J. Am. Ceram. Soc., 50(2), (1967) p. 113.

8) C.D. Wirkus, M.F. Berard and D.R. Wilder, J. Am. Ceram. Soc., 51(11), (1968) p. 643.

9) K. Ando, Y. Oishi and H. Hase, J. Am. Ceram. Soc. Communications, 66(12) (1983) p. c222.

10) R.J. Gabroriaud, J. Solid State Chem., 35 (1980) p. 252.

11) K.T. Faber, M.D. Huang and A.G.Evans, J.Am. Ceram. Soc., 64(5) (1981) p. 296.

12) "Handbook on the Physics and Chemistry of Rare Earths" K.A. Gshneider Jr., L. Eyring ed., Vol.3, North Holland, Amsterdam, Netherlands (1979)

13) M.G. Paton and E.N. Maolen, Acta Cryst., 19 (1965) p. 307.

14) A.F. Wells, "Structural Inorganic Chemistry", 5th edition, Claredon Press, Oxford (1984) p. 543.

15) L.M. Lopato, Ceramurgia Int., 2(1) (1976) p. 18.

16) L.M. Lopato et al., Russ. J. Phys. Chem, 47(3) (1973) p. 352.

17) S.G. Tresvyatski et al., Izv. Akad. Nauk. SSSR, Neorg Mat., 7(11) (1971) p. 2020.

18) L.M. Lopato et al., Dopov. Akad. Nauk. Ukr. RSR. series B, 32(12) (1970) p.1106.

19) L.M. Lopato et al., Izv. Akad. Nauk. SSSR, Neorg Mat. 9(3) (1973) p. 427.

20) T L. Barry et al., J. Am. Ceram. Soc., 49(12) (1966) p.667.

21) F. Queyroux, Rev. Int. Hautes Temper. et Refract., 2(4) (1965) p.311.

22) T.H. Etsell, "The Electrical Properties of La_2O_3-CaO, Y_2O_3-CaO, and ZrO_2-CaO Solid Electrolytes", PHD Thesis University of Toronto, 1969.

23) L.M. Lopato, I.M. Maister and A.V. Shevchenko, Izv. Akad Nauk. SSSR, Neorg. Mat., 8(5) (1972) p.861.

24) L.M. Lopato et al., Zh. Neorg. Khim., 20(7) (1975) p.1970.

25) S.G Tresvyatskii et al., Izv. Akad. Nauk. SSSR, Neorg. Mat., 7(10) (1971) p. 1808.

26) L.M. Lopato and A.V. Shevchenko, Izv. Akad. Nauk. SSSR, Neorg. Mat., 15(6) (1979) p. 996.

27) L.M. Lopato, Izv. Akad. Nauk. SSSR, Neorg. Mat., 20 (1984) p. 972.

28) N.M. Tallon and R.W. Vest, J. Am. Ceram. Soc., 49(8) (1966) p. 401.

29) W. Noddack and H. Walch, Z. Phys. Chem. (Leipzig). 231 (1959) p.180.

30) E.G. Subba Rao, P.H. Sutter and J. Hrizo, J. Am. Ceram. Soc., 48(9) (1965) p.46.

31) V.B. Tare and H. Schmalzried, Z. Phys. Chem. (NF). 43 (1970) p. 377.

32) C.C. McPheeters, J.C. McGuire. U.S. Patent # 3.309.233 March 14. 1967.

33) J.Schieltz, J.W. Patterson and D.R. Wilder, J. Electrochemical Soc., 118(7) (1971) p. 1140.

34) Z.S. Volchenkova and D.S. Zubankova. Izv. Akad. Nauk. SSSR, Neorg. Mat., 12(9) (1976) p. 1695.

35) B.C.H. Steele and P.M.R. Moody, Proc. Br. Ceram. Soc., 10 (1968) p. 87.

36) K.H. Kim, J.H. Jun and J.S. Chai, J. Phys. Chem. Solids 46(10) (1985) p. 1173.

37) K. Uematsu et al., J. Am. Ceram. Soc., 62 (1979) p.219.

38) H.G. Scott. J. Materials Science, 12 (1977) p. 311.

39) A. Biggs, D.F. Dailly and B.E. Waye, Proc. Br. Ceram. Soc., 23 (1972) p. 44.

40) V.S. Stubican and R.Roy, J. Phys. Chem. Solids, 26 (1965) p.1293.

41) V.S. Stubican and D.J. Viechnicki, J. Applied. Phys., 37 (1966) p.2751.

42) D.E. Smith, T.Y. Tien, H.Van Vlack. Ceramic Microstructures. Proc. Int. Mater. Symp. 6th, Westview Press. Boulder, Co., USA.,1976 p. 330.

43) T.L. Barry, V.S. Stubican, and R. Roy, J. Am. Ceram. Soc., 50(7) (1967) p. 375.

44) J. Beretka, J. Am. Ceram. Soc., 67(9) (1984) p. 615.

45) J.D. Hawcook and J.H. Sharp, J. Am. Ceram. Soc. 55(2) (1972) p. 74.

46) F.A. Kroeger. "The Chemistry of Imperfect Crystals" North Holland, Amsterdam (1964).

47) D.A. Porter and K.E. Easterling, "Phase Transformations in Metals and Alloys", Van Nostrand Reinhold, Wokingham, England (1981).

48) C. Zener, Journal of Applied Physics, 20(10) (1949) p. 950.

49) H. Schmalzried, "Solid State Reactions" Monographs in Modern Chemistry 12. Verlag Chemie, Weinheim. West Germany, 1981.

50) A. Ziabicki, Journal of Chemical Physics, 48(10) (1968) p. 4368.

51) A. Ziabicki, Journal of Chemical Physics, 48(10) (1968) p. 4374.

52) A. Ziabicki, Journal of Chemical Physics, 66(7) (1977) p. 1638.

53) A. Ziabicki. Journal of Chemical Physics. 85(5) (1986) p. 3042.

54) M. Avrami. Journal of Chemical Physics. 7 (1939) p.1103.

55) B.V. Erofe'ev, Compt. rend. Acad. Sci.. U.S.S.R 52 (1946) p.511.

56) M.E. Fine. "Phase Transformations in a Condensed System" MacMillan Co. (1964) p. 47.

57) J.W. Christian, "The Theory of Transformations in Metals and Alloys", Pergamon Press, New York (1965) p. 471.

58) S.F. Hulbert. J. Br. Ceram. Soc., 6(1) (1969) p.11.

59) B.D. Cullity. "Elements of X-Ray Diffraction", 2nd edition. Addison-Wesley Publ., Reading, Mass., (1978).

60) W.D. Kingery. "Introduction to Ceramics", John Wiley and Sons, New York (1960).

61) ASTM Powder Diffraction Files. American Society for Testing and Materials. Sets 1-5. (1967).

62) M. Foex and J.P. Traverse. Rev. Int. Hautes Temper. et Refract.. 3(4) (1966) p.429.

63) T. Norby and P. Kofstad, Solid State Ionics, 20 (1986) p. 169.

64) T. Norby and P. Kofstad, J. Am. Ceram. Soc., 69(11) (1986) p. 780.

Appendix I

The powder diffraction card files for Y_2O_3 and CaO [*1]

d	3.06	1.87	1.60	4.34	Y_2O_3
I/I_1	100	46	31	16	YTTRIUM III OXIDE

Rad. Cu λ 1.5405 Filter Ni
Dia. Cut off Coll.
I/I_1 G. C. DIFFRACTOMETER d corr. abs.?
Ref. SWANSON AND FUYAT, NBS CIRCULAR 539, VOL. III (1953)

Sys. CUBIC (BODY-CENTERED) S.G. T^6 - $I2_13$
a_o 10.604 b_o c_o A C
α β γ Z 16
Ref. IBID.

εα nωβ>1.77 εγ Sign
2V D 5.657 mp Color
Ref.

SAMPLE FROM THE NBS SPEC. LAB. SPECT. ANAL.: <0.1% Ba; <0.01% Ca, Eu, Si; <0.001% Mg, Pb, Yb.
X-RAY PATTERN AT 27°C.

REPLACES 1-0831

d Å	I/I_1	hkl	d Å	I/I_1	hkl
4.34	16	211	1.443	3	721
3.060	100	222	1.417	2	642
2.652	30	400	1.346	2	732
2.500	7	411	1.325	4	800
2.372	1	420	1.305	3	811
2.261	8	332	1.287	1	820
2.165	1	422	1.267	2	653
2.080	12	510	1.249	1	822
1.936	3	521	1.233	3	831
1.874	46	440	1.216	8	662
1.818	2	530	1.1854	5	840
1.769	<1	600	1.1708	1	910
1.720	5	611	1.1570	1	842
1.677	1	620	1.1436	2	921
1.636	4	541	1.1178	2	930
1.599	31	622	1.0939	2	932
1.563	7	631	1.0821	5	844
1.531	5	444	1.0711	2	941
1.499	2	710	1.0606	1	10.0.0
1.470	1	640	1.0499	<1	10.1.1

d 4-0777	2.41	1.70	2.78	2.778	CaO
I/I_1 4-0777	100	45	34	34	CALCIUM OXIDE (LIME)

Rad. $CuK\alpha_1$ λ 1.5405 Filter Ni
Dia. Cut off 50 Coll.
I/I_1 G. C. DIFFRACTOMETER d corr. abs.?
Ref. SWANSON AND TATGE, J. C. FEL. REPORTS, NBS (1950)

Sys. CUBIC S.G. O_h^5 - $Fm3u$
a_o 4.8105 b_o c_o A C
α β γ Z 4
Ref. IBID.

εα nωβ 1.837 εγ Sign
2V D 3.345 mp (WA) Color
Ref. (NBS)

NBS ANALYSIS SHOWS ABOUT 0.21% MgO, 0.1% Ba, AND NO OTHER IMPURITY OVER 0.04%
AT 27°C
TO REPLACE 1-1160, 2-1089, 3-1123

d Å	I/I_1	hkl	d Å	I/I_1	hkl
2.778	34	111			
2.405	100	200			
1.701	45	220			
1.451	10	311			
1.390	5	222			
1.203	4	400			
1.1036	4	331			
1.0755	9	420			
0.9819	9	422			
.9258	3	511			
.8504	4	440			
.8131	5	531			
.8018	6	600			